Multiscale model of the role of grain boundary structures in the dynamic intergranular failure of polycrystal aggregates

Andres F. Galvis[1]*, Pedro A. Santos-Flórez[2], Paulo Sollero[1], Maurice de Koning[2], Luiz C. Wrobel[3,4]

[1]*School of Mechanical Engineering, University of Campinas, Campinas 13083-860, SP, Brazil.*
[2]*Gleb Wataghin Institute of Physics, University of Campinas, Campinas 13083-859, SP, Brazil.*
[3]*College of Engineering, Design and Physical Sciences, Brunel University London, Uxbridge UB8 3PH, UK.*
[4]*Department of Civil and Environmental Engineering, Pontifical Catholic University of Rio de Janeiro, Rio de Janeiro 22451-900, Brazil*

Abstract

A multiscale approach to investigate the influence of the grain boundary (GB) lattice structures on the dynamic intergranular failure in 3D polycrystalline materials is proposed. The model comprises the meso- and atomistic scales using the boundary element method (BEM) and molecular dynamics (MD), respectively. At the mesoscale, stochastic grain morphologies, random crystalline orientations and initial defects are included in the physical model. Moreover, a dynamic high-rate load is imposed to produce dynamic stress and strain waves propagating throughout the polycrystal, inducing the material to be susceptible to fail. The intergranular failure is governed by the critical energy density for shear and cleavage modes, evaluated from a set of nano GBs at the atomistic scale. The novelty is the assessment of the energy density considering its dependency on the interface

*Corresponding author
Email address: andres.galvis@fem.unicamp.br (Andres F. Galvis[1])

lattice, leading to a group of failure criteria distributed along the aggregate. The difference in the order of magnitude between these length scales is a challenge for the transition multiscale model. Hence, an asymptotic scaling methodology is adapted for bridging the mechanical strength. Finally, it is worth noting that the level of detail of this criterion, is a remarkable enhancement over other intergranular failure models.
Keywords: Multiscale, Dynamic failure, Energy density, Boundary element method, Molecular dynamics.

1. Introduction

Many industrial developments and applications use metallic materials in their components, basically designed to prevent failure that could lead to the collapse of the overall system. Additional to the optimal geometrical design, the material behavior takes place on the configuration in the limits of the imposed environmental and boundary conditions. Important physical effects can be captured when very small length scales are considered in the analysis, such as strong variations in the geometrical morphology, material properties, and defects that are observed when a microscale analysis is taken into account. Improvements in failure analyses can be achieved including the microscale behavior through bridging scale transitions. Moreover, the atomistic scale can be considered in order to obtain a more realistic failure modeling of the mesoscale.

Microscopically, polycrystal metallic materials are composed of randomly oriented crystal aggregates. From the macroscale, each material point is represented by an aggregate of non-periodic polycrystals. Then, the macroscopic elastic properties are statistically approximated by the assembly of random mor-

phology grains with their own crystalline orientations. The constitutive model of each grain is usually assumed as an anisotropic elastic medium, where the elastic properties depend on the lattice structure, e.g. cubic or hexagonal crystals, and interatomic potentials. It is a difficult task to reproduce artificial polycrystalline structures owing to their random morphology. The mesh generation is a critical task to adequately model polycrystalline materials. Several techniques such as experimental image reconstruction, Voronoi and Laguerre tessellation meshing, and re-meshing are, in particular, useful for non-periodic polycrystalline aggregates. Computational frameworks to build polycrystalline structures can be found in the literature. The most common is the Voronoi tessellation for artificial structures as Voro++ [1] and Neper [2]. Several schemes were presented to discretize the Voronoi structure, like superficial meshes for boundary elements [3] and volumetric meshes [4, 5] to be used with finite element method (FEM). As the mechanical response is required and in this research the BEM is implemented, it will be assessed by the displacement and traction fields using the 3D fundamental solution for general anisotropic materials proposed by [6]. In this case, the displacement field is represented by double Fourier series, offering the possibility to evaluate its coefficients once for each crystalline orientation. Hence, this fundamental solution represents an advantage for the analysis, because a database of Fourier coefficients can be generated for each material, considering a large number of different crystalline orientations.

According to the aforementioned description of the material at the microscale, the mechanical behavior of each grain surface should be assessed. Hence, the BEM benefits this model by evaluating the high stress and strain gradients by only using the surface discretization of each grain in the polycrystalline aggre-

gate. The mesoscale model considers the interfaces as perfect flat surfaces where the analysis is conducted applying traction equilibrium and displacement compatibility through the multidomain analysis. The grain boundaries (GBs) constitute the transition planes of the two adjacent crystalline orientations, being an important object of study for intergranular failure analysis. At the macroscale, metallic materials have the tendency to isotropy when the number of grains is sufficiently large. As a validation of the elastostatic BEM formulation, a convergence analysis of the effective macroscopic elastic properties was previously presented in [7] based on the strategies depicted in [4, 8]. Reliable results were obtained, showing the macroscopic isotropic trend when more grains are contained in the microvolume.

The application of dynamic loads with a rapid rate of change over time leads to other physical considerations when compared with static or quasi-static models. The high-rate load conditions turn the mechanical fields dependent on the inertial force, which resists the acceleration induced in the body. These physical effects are the main characteristic of dynamics problems [9], where the dynamic deformation due to high-rate loads should be analyzed. In this case, there is a high strain gradient in a part of the body, and the remaining parts do not yet experience stresses, because strain and stress waves propagate through the solid at a specified velocity [10]. Dynamic loads play an important role in failure analysis, as the material is more susceptible to fail under impulsive or high-rate strain loads, which affects the fracture behavior [11], making necessary a dynamic fracture mechanics analysis [12]. A computational framework for validating the dynamic 3D anisotropic model was previously presented in [13] using the elastodynamic BEM formulation. Notably, results were achieved showing the degradation in the

numerical response when the simulation time increases.

Failure analyses have advanced from conventional fracture mechanics and cohesive models. Nowadays, there are several numerical studies of brittle intergranular and transgranular failure of 3D polycrystalline materials, through the measurement of the mechanical degradation using approaches such as cohesive zone models (CZM) [3], quasi-continuum methods [14] or homogenized atomistic-continuum techniques [15]. This work focuses on the intergranular failure process in multiscale atomistic-continuum modeling of GBs. In the atomistic scale, the GB model regards the transition structure produced by the collapse of two adjoining interior grain lattices. It is widely known that the atomistic media is governed by the thermodynamic state and the force field. Moreover, the potential energy serves to identify the more susceptible failure structures. In the interfaces that contain a high quantity of defects, owing to the broken bonds of the transition lattice, high potential energy reflects a failure interface zone. The failure is characterized by the critical energy density atomistically assessed for different modes, using the generalized energy failure criterion proposed by Qu et al. [16]. This criterion offers a straightforward way to evaluate failure at the microscale, taking into account a certain mixed level of ductile and brittle failure occurring in the interface. Due to the lack of available data of the critical energy densities for cleavage and shear modes, an MD model of GBs is implemented. Additionally, using this strategy, the failure criterion is extended to consider the variation in the lattice structures in the interfaces. Finally, due to the nature of metallic materials in its mesoscale, flaws, and defects such as intergranular cracks are contained in the polycrystalline structure. These initial defects act as potential weak zones where the failure could initiate.

In the analysis through different length scales, the mechanical properties of materials vary owing to their size and rate dependence. As the length scale increases, the magnitude of the failure stress drastically decreases. Further, as shown in [17], the yield stress decreases with the specimen size and increases with the strain rate. Hence, the bridging approach to obtain the critical failure mechanisms at the mesoscale represents a challenge that is worthy of investigation. For this purpose, the stress-strain curves obtained at the nanoscale will be transferred to the mesoscopic domain. There is also an additional limitation due to the lack of available experimental data at nanoscopic GBs, in where MD modeling becomes a powerful numerical approach to obtain atomistic failure behavior. In real material observations at the nanoscale, the yield stress limit occurs mainly for the nucleation of dislocations in the material. Therefore, a larger size of material can result in a higher chance for nucleating the dislocation, which yields lower initial stress [18, 19]. Guo et al. [19] showed for copper and nickel that a critical strain-rate exists, below which the yield stress becomes nearly constant. They also analyzed the length scale dependence, which as mentioned affects the yield strength. All the cited studies developed their results considering bulk lattice structures. Another approach presented by Hammami and Kulkarni [20], used grain boundary sliding in nanostructures to investigate the rate dependence using atomistic simulations. They obtained similar results of the rate dependence of mechanical properties for a *tilt* GB of aluminum. For larger scales, the scaling of properties is based on a continuum formulation of the geometrically necessary dislocations to produce plastic strain; some classical and recognized publications treating these phenomena are [21, 22]. A useful formulation was presented by Chen et al. [23, 24]. They developed the hypersurface that combines strain-rate

and the specimen size effects on material properties, and also showed functions to represent the size effect that are used in this work after some assumptions.

This research presents a multiscale scheme to analyze the dynamic intergranular failure in 3D polycrystalline materials. The model contains the meso- and atomistic scales using BEM and MD, respectively. The BEM formulation used a small strain assumption without any thermal effect and the dynamic analysis of the polycrystal aggregate considers crack initiation at the micro-domain. As mentioned, the failure propagates according to the criterion defined by the critical energy densities at the interfaces. In order to apply the failure criterion in the mesoscale properly, an asymptotic analysis is adapted to scale the mechanical properties from the nano and micro scales. The main BEM application is implemented in Fortran 90, parallelized on a distributed architecture memory using MPI. The atomistic evaluation of the critical energy densities is carried out from the model of the GB as a bicrystal. This gives a detailed physical description of the atomistic arrangement at the interface differing from the structure inside the adjacent grains. Hence, GB categories given by the coincident-site lattice (CSL) model are employed to construct a statistical sample of *tilt* and *twist* GBs, Fig. 1.

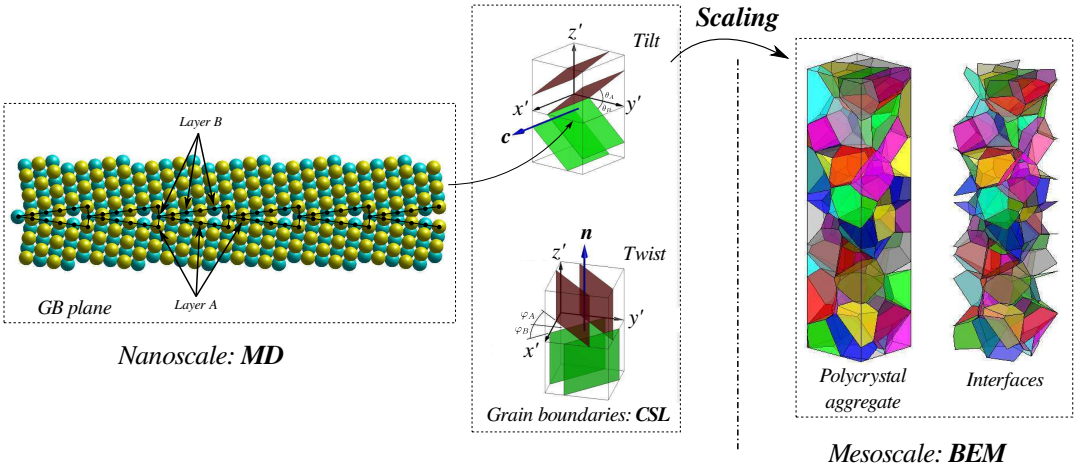

Figure 1: Multiscale approach.

In the understanding provided by atomistic modeling of Fe grain boundaries, the resulting lattice structure at the GB plane caused by the collapse of two adjacent grains differs from the atomic lattice within the bulk material or non-boundary region. Then, the presence of the GB is considered as a defect or imperfection in the nano-specimen. From an energy minimization point of view, as shown in Section 3, it is demonstrated the influence of the GB defects on the material weakness compared to a perfect material with the same number of atoms. Hence, at the atomistic level, failure for both tensile and shear modes will always occur at the GB plan. Further, by the difference between the strength of the interfaces and bulk material, the aggregate tended to fail at the interface zone. Moreover, for fine-grained iron (grain size less than 10 um), GBs defects become the reason of onset intergranular failure throughout the polycrystal structure.

This multiscale framework offers the possibility to combine the nano- and meso- scales even considering the representative difference in their characteristic lengths. Additional physical phenomena were captured on the continuum

mesoscale by the incorporation of the nanoscale modeled using MD. It was demonstrated how the failure processes at interfaces have a relevant influence caused by the resulting lattice structures after two adjacent grains are atomistically collapsed. This fact is considered the enhancement and novelty of this dynamic failure model compared with others in the literature. Therefore, this is a proper approach from a continuum point of view, where the interface failure criteria were generated with the mentioned considerations. For simulating failure in metallic materials from a microscopic standpoint, the proposed model intends harnessing what BEM and MD can provide at each scale. It would be very expensive in terms of computational cost if MD simulations are carried out generating a complete atomic polycrystalline aggregate with a grain size of about $10\,\mu$m. On the other hand, a pure continuum simulation by itself would have a dependency on experimental data for modeling the failure of several metals. Then, the synergy of these methods provides a proper approach for the analysis of polycrystals with large grain size, even with the level of detail offered by the atomistic modeling.

The atomistic analysis of failure contemplates annealing and quenching processes, in which the bicrystal relaxation and the dynamic evolution of the system under high-rate deformation boundary conditions are simulated using the Large-scale Atomic/Molecular Massively Parallel Simulator (LAMMPS) [25]. Thus, the critical energy density is derived from the constitutive relationship between the strain and the Virial stress tensors. Due to the incorporation of the atomistic behavior, which considers the broken bonds formed in the GBs at the interfaces, the overall multiscale approach attempts to model a more realistic intergranular failure condition.

2. Polycrystal aggregate model

Macroscopically, metallic materials are homogeneous and isotropic solids, facilitating the investigations of failure theories that give reliable results in large scales. These materials contain a high quantity of heterogeneities from a microscopic point of view. Defects such as nano-cracks, voids, secondary-phase impurities appearing in the interfaces are considered an important object of study. As the length scale increases, more defects are included in the domain, degrading the overall mechanical behavior. Microscopically, it is found that the material is constituted by the collective assembly of crystal grains produced by the nucleation of the solidification in the fabrication process. Although the lattice structure of a particular grain with a proper crystalline orientation remains constant, localized defects as vacancies or dislocations could also occur in the bulk material, especially when the grain-size is large. At the mesoscale, these materials have a highly stochastic and morphological character and as the number of grains increases, the homogenized macroscopic elastic properties tend to isotropy as statistically shown for different metals in [7]. This allows the use of an artificial polycrystal structure as shown in Fig. 2, to guarantee the reproducibility of the macroscopic constitutive behavior, where random grain size, morphology, and flat interfaces are contemplated.

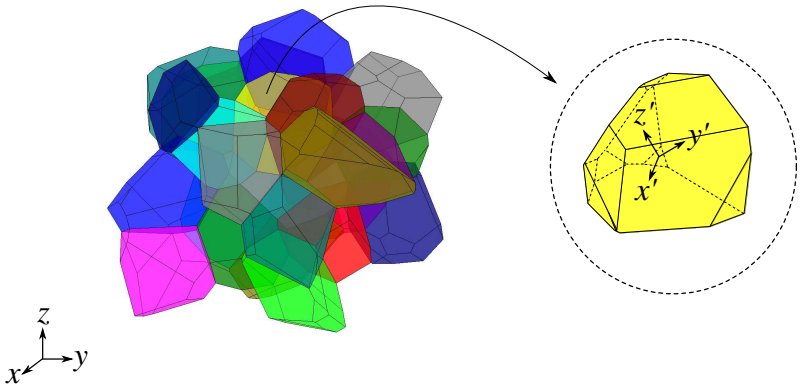

Figure 2: Polycrystal aggregate.

The structure is built using 3D Voronoi tessellation and discretized with triangular elements. In this work, the hierarchical procedure implemented with *C*++/C, illustrated by Galvis et al. [7] is employed. The algorithm is composed by the *V*oro++ [1, 26, 27] and the *Triangle* mesh generator [28] libraries. This strategy offers the possibility to build meshes with different levels of refinement, essential to obtain an adequate resolution for failure simulations. Being the reference stiffness elastic properties $\mathbf{C} \equiv C_{ijkl}$ at the global coordinate system (x, y, z), different crystalline orientations represented by $\mathbf{C}'$ are obtained at the local coordinate system (x', y', z') applying the classical rotation procedure described in [29]. Then, the random distribution of crystalline orientations along the aggregate will be accounted by the random stiffness tensors $\mathbf{C}'_i$, where $i = 1, 2, ..., N_{gr}$ being N_{gr} the number of grains in the specimen. In this work, it is assume as recommended by Fritzen el at. [4] and used in [7, 13] that the grain orientations in the polycrystal aggregate are uniformly distributed over the group of rotations based on a nonlinear transformation of Euler angles ($z - x - z$convention), being θ_x and θ_z random angles.

Now, the constitutive model of polycrystalline materials is defined. The next step is the correct evaluation of the mechanical fields when quasi-static or dynamic boundary conditions are imposed. The BEM formulation requires a fundamental solution for 3D anisotropic solids. It quantifies the response of the continuum medium at the field point $\mathbf{x}$, by a perturbation applied at the source point $\mathbf{x}'$ through the Green's function $\mathbf{U}(\mathbf{x},\mathbf{x}')$ expressed in terms of the Barnett-Lothe tensor [30, 31] $\mathbf{H}(\theta,\phi)$ shown in Eq. (1), where θ and ϕ are the spherical coordinates of a vector built from $\mathbf{x}'$ to $\mathbf{x}$. The reader is referred to the work published by Ting and Lee [32], where its geometrical and explicit mathematical expressions are explained in detail.

$$\mathbf{U}(r,\theta,\phi) = \frac{1}{4\pi r}\mathbf{H}(\theta,\phi) \quad . \tag{1}$$

In Eq. (1), r is the distance between the source point $\mathbf{x}'$ located at the origin and the field point $\mathbf{x}$. A more explicit way to evaluate the Barnett-Lothe tensor $\mathbf{H}(\theta,\phi)$ is expressed in terms of the Stroh's eigenvalues q_n as

$$\mathbf{H}(\theta,\phi) = \frac{1}{|\boldsymbol{\kappa}|}\sum_{n=0}^{4} q_n \hat{I}^{(n)} \quad . \tag{2}$$

The expressions to evaluate the $\boldsymbol{\kappa}$ and $\hat{I}^{(n)}$ are presented in detail in [6, 7]. They depend on the stiffness tensor $\mathbf{C}_i$. For every set of spherical angles (θ,ϕ) in the anisotropic medium, after mathematical reductions, $\mathbf{H}(\theta,\phi)$ is expressed as a contour integral around a unit circle at the field point $\mathbf{x}$ on an oblique plane normal to the $\overline{\mathbf{x}'\mathbf{x}}$ vector, see details in [7]. In this work, the evaluation of the fundamental solution was implemented using the scheme proposed by Tan et al. [6]. Due to the periodic characteristic of $\mathbf{H}(\theta,\phi)$, the representation in terms of double Fourier

series around θ and ϕ is given by

$$H_{ij}(\theta,\phi) = \sum_{m=-\alpha}^{\alpha}\sum_{n=-\alpha}^{\alpha} \lambda_{ij}^{(m,n)} e^{\mathbf{i}(m\theta+n\phi)} \, (i,j=1,2,3) \quad , \tag{3}$$

where α is an appropriately large integer for convergence of the series, α represents the number of Gauss points and their corresponding weights. According to Tan et al. [6], a value of α greater than 32 is recommended for highly anisotropic materials. The unknown Fourier coefficients $\lambda_{ij}^{(m,n)}$ are given by

$$\lambda_{ij}^{(m,n)} = \frac{1}{4\pi^2}\int_{-\pi}^{\pi}\int_{-\pi}^{\pi} H_{ij}(\theta,\phi) e^{-i(m\theta+n\phi)} d\theta d\phi \quad . \tag{4}$$

Note in Eq. (4), the straightforward way to evaluate the Fourier coefficients $\lambda_{ij}^{(m,n)}$ using the auxiliary explicit form of $H_{ij}(\theta,\phi)$ shown in Eq. (2). In short, substituting Eq. (4) into Eq. (1), the displacement fundamental solution can also be expressed by Eq. (5).

$$U_{ij}(r,\theta,\phi) = \frac{1}{4\pi r}\sum_{m=-\alpha}^{\alpha}\sum_{n=-\alpha}^{\alpha} \lambda_{ij}^{(m,n)} e^{\mathbf{i}(m\theta+n\phi)} \, (i,j=1,2,3) \quad . \tag{5}$$

It is worth noting that using this formulation, the Fourier coefficients $\lambda_{ij}^{(m,n)}$ are calculated only once for each $\mathbf{C}_i'$, $i = 1,2,...N_{gr}$ and saved in a separated database, this procedure was widely described in [7, 33]. Then, for each $\mathbf{C}_i'$, the results of this contour integral will give the (θ,ϕ) independent terms of $\lambda_{ij}^{(m,n)}$ [6, 33]. Finally, the Eq. (1) can be applied for every material point in the solid. The problem of anisotropic elasticity can now be solved, with the solutions of the fundamental problem and the well-known boundary integral equation (BIE) as follows:

$$c_{ik}u_i + \int_{\Gamma^{\mathrm{g}}} T_{ik}u_i \, \mathrm{d}\Gamma = \int_{\Gamma^{\mathrm{g}}} U_{ik}t_i \, \mathrm{d}\Gamma + \int_{\Omega^{\mathrm{g}}} \rho\ddot{u}_i U_{ik} \, \mathrm{d}\Omega \quad , \tag{6}$$

where c_{ik} is $\delta_{ik}/2$ for a source point located at the surface boundary, being δ_{ik} the Kronecker delta and ρ the mass density. In Eq. (6), $\Gamma^{\mathfrak{g}}$ and $\Omega^{\mathfrak{g}}$ indicate the integration over the grain $\mathfrak{g}$ surface and domain respectively. U_{ik} and T_{ik} represent the fundamental solutions of displacement and tractions, respectively, in the i-direction of the field point $\mathbf{x}$ due to a unit load in the j-direction at the source point $\mathbf{x}'$ in a homogeneous infinite body. The traction fundamental solution T_{ik} can be evaluated from U_{ik} by the Cauchy's theorem and Hooke's law as shown in [6]. Finally, u_i and t_i are the displacement and traction on the surface $\Gamma^{\mathfrak{g}}$. For transient analysis, the body forces are caused by the acceleration field $\ddot{u}_i$. The domain integral considers the terms of the dynamic effects. In order to apply the BEM formulation, it is required the transformation of this domain integral into a boundary or surface integral. In this work, the dual reciprocity boundary element method (DRBEM) is implemented to deal with the transformation. The DRBEM has been employed in applications such as polycrystalline materials [13], fiber composites [34] and piezoelectric materials [35]. In these publications and in the references therein, the procedure to find the general BIE, Eq. (7), in terms of surface integral is shown.

$$c_{ik}u_i + \int_{\Gamma^{\mathfrak{g}}} T_{ik}u_i \mathrm{d}\Gamma = \int_{\Gamma^{\mathfrak{g}}} U_{ik}t_i \mathrm{d}\Gamma + \sum_{j=1}^{M} \alpha_n^j \left\{ c_{ik}\hat{u}_{kn}^j - \int_{\Gamma^{\mathfrak{g}}} U_{ik}\hat{t}_{kn}^j \mathrm{d}\Gamma + \int_{\Gamma^{\mathfrak{g}}} T_{ik}\hat{u}_{kn}^j \mathrm{d}\Gamma \right\} \quad . \tag{7}$$

In Eq. (7), α_n^j represents unknown coefficients that are function of (M) radial expressions and are related to the body force term $\rho\ddot{u}_i$, see details in [13, 36]. The $\hat{u}_{in}^m$ term is called a particular solution and is usually a radial function [35]

expressed as

$$\hat{u}_{kn} = \delta_{kn}(r^2 + r^3) \quad , \tag{8}$$

and its derivatives

$$\begin{aligned} \hat{u}_{kn,l} &= \delta_{kn}(2r + 3r^2)r_{,l} \quad , \\ \hat{u}_{kn,lj} &= \delta_{kn}\left[(2 + 3r)\delta_{lj} + 3rr_{,j}r_{,l}\right] \quad . \end{aligned} \tag{9}$$

being r the norm of the $\overline{\mathbf{x}'\mathbf{x}}$ vector. The particular solution $\hat{t}^j_{kn}$ can be evaluated using Eq. (8) and Cauchy's theorem. The k and n indices of the particular solutions work in the same manner as the i and k index of the fundamental solutions. Equation (7) must be discretized into surface elements, where linear three-node discontinuous triangular boundary elements are used [33]. The feature of these elements is that they have three nodes inside the element. The main reasons to use this type of boundary elements are: (i) the facility in the implementation of the mesh generator, (ii) linear elements represent a drastic reduction in the number of degrees of freedom (DOF) and the computational cost required by the numerical integration and (iii) discontinuous elements offer advantages in the implementation of the multidomain algorithm. Due to the nature of this application, there are no shared nodes by more than two grains of the polycrystal aggregate, because these elements have three nodes inside the element [33]. Then, one node at the interface is shared by no more than two grains. After the discretization, the BIE in its matrix form is

$$\mathbf{M}\ddot{\mathbf{u}} + \mathbf{H}\mathbf{u} = \mathbf{G}\mathbf{t} \quad , \tag{10}$$

where

$$\mathbf{M} = \left(\mathbf{G}\hat{\mathbf{T}} - \mathbf{H}\hat{\mathbf{U}}\right)\boldsymbol{\alpha} \quad . \tag{11}$$

Matrices **G** and **H** result from the integration of the traction and displacement fundamental solutions, respectively. **M** in Eq. (11), is defined as the mass matrix and contains the mass density ρ, the matrix of radial functions $\boldsymbol{\alpha}$ and the integration matrices of the particular solutions $\hat{\mathbf{T}}$ and $\hat{\mathbf{U}}$, Eq. (11). For the definition of matrices **H**, **G** and **M**, the reader is referred to [7, 13, 33], where a detailed description of the discretization steps to obtain Eq (10) from Eq (7) is presented.

Additionally, if a high-rate boundary condition is applied on the microstructure, stress and strain waves propagate through the aggregate. Initially, in a small time after the application of the high-rate condition and only a portion of the structure experiments the stresses. It produces a non-linear deformation gradient where the strain is not constant because of the stress wave across the solid. These inertial and transient effects were explored by Galvis et al. [7] for different inputs such as Heaviside, ramp and harmonic high-rate loads. Hence, Eq. (10) is integrated over time using the Houbolt algorithm [37], which is the most popular scheme in this BEM formulation [38, 39]. The evolution of Eq. (10) over time is obtained at every instant $\tau + \Delta\tau$, where the acceleration of the body can be expressed in terms of the last three-time steps using finite differences as

$$\ddot{\mathbf{u}}_{\tau+\Delta\tau} = \frac{1}{\Delta\tau^2}\left(2\mathbf{u}_{\tau+\Delta\tau} - 5\mathbf{u}_{\tau} + 4\mathbf{u}_{\tau-\Delta\tau} - \mathbf{u}_{\tau-2\Delta\tau}\right) \quad , \tag{12}$$

writing Eq. (10) at instant $\tau + \Delta\tau$

$$\mathbf{M}\ddot{\mathbf{u}}_{\tau+\Delta\tau} + \mathbf{H}\mathbf{u}_{\tau+\Delta\tau} = \mathbf{G}\mathbf{t}_{\tau+\Delta\tau} \quad , \tag{13}$$

and by the substitution of Eq. (12) into Eq. (13) leads to Eq. (14)

$$\left[\frac{2}{\Delta\tau^2}\mathbf{M}+\mathbf{H}\right]\mathbf{u}_{\tau+\Delta\tau}=\mathbf{G}\mathbf{t}_{\tau+\Delta\tau}+\frac{1}{\Delta\tau^2}\mathbf{M}(5\mathbf{u}_{\tau}-4\mathbf{u}_{\tau-\Delta\tau}+\mathbf{u}_{\tau-2\Delta\tau}) \quad , \tag{14}$$

where the vectors $\mathbf{u}_{\tau+\Delta\tau}$ and $\mathbf{t}_{\tau+\Delta\tau}$ are the displacement and traction fields at the instant $\tau+\Delta\tau$, respectively. Polycrystalline structures require the implementation of an algorithm to numerically assemble all the grains into the overall domain. Hence, the created interfaces between adjacent grains are modeled by the application of simple displacement compatibility and traction equilibrium conditions shown in the following equation

$$\begin{aligned}\mathbf{u}^i&=\mathbf{u}^j \quad ,\\ \mathbf{t}^i&=-\mathbf{t}^j \quad ,\end{aligned} \tag{15}$$

being the superscripts i and j indices represent the ith and jth adjacent grains. The multidomain algorithm divides the matrices into blocks. The first corresponds to the elements where the boundary conditions bc are applied in the grain $\mathfrak{g}$ in the external surfaces of the overall specimen, defined as $\mathbf{A}^{\mathfrak{g}}$ and $\mathbf{B}^{\mathfrak{g}}$ for known displacement and tractions, respectively, as follows

$$\mathbf{A}^{\mathfrak{g}}=\left[\frac{2}{\Delta\tau^2}\mathbf{M}^{\mathfrak{g}}_{bc}+\mathbf{H}^{\mathfrak{g}}_{bc}\right], \quad \mathbf{B}^{\mathfrak{g}}=\mathbf{G}^{\mathfrak{g}}_{bc} \quad , \tag{16}$$

where $\mathbf{H}^{\mathfrak{g}}_{bc}$ and $\mathbf{G}^{\mathfrak{g}}_{bc}$ are the blocks after the exchange of columns where known displacement boundary conditions are imposed. $\mathbf{M}^{\mathfrak{g}}_{bc}$ contains the same columns of $\mathbf{H}^{\mathfrak{g}}_{bc}$ corresponding to the known displacement conditions. For the internal elements that belong to the interfaces $\mathcal{I}$, the block matrix is defined by $\mathbf{F}^{\mathfrak{g}}$ and

evaluated as

$$\mathbf{F}^{\mathfrak{g}} = \left[\frac{2}{\Delta\tau^2}\mathbf{M}_{\mathcal{I}}^{\mathfrak{g}} + \mathbf{H}_{\mathcal{I}}^{\mathfrak{g}} \right] \quad , \tag{17}$$

being $\mathbf{H}_{\mathcal{I}}^{\mathfrak{g}}$ and $\mathbf{M}_{\mathcal{I}}^{\mathfrak{g}}$ the blocks of corresponding columns of the nodes at the interface $\mathcal{I}$. Finally, the vector containing the displacement information of the last three time steps is defined by

$$\mathbf{u}_{\alpha}^{\mathfrak{g}} = \frac{1}{\Delta\tau^2}\left(5\mathbf{u}_{\tau}^{\mathfrak{g}} - 4\mathbf{u}_{\tau-\Delta\tau}^{\mathfrak{g}} + \mathbf{u}_{\tau-2\Delta\tau}^{\mathfrak{g}}\right) \quad . \tag{18}$$

If a single interface between two adjacent ith and jth grains is considered, the final system of equations will take the following configuration

$$\begin{bmatrix} \mathbf{A}^i & \mathbf{F}_i^j\mathbf{R}^i & -\mathbf{G}_i^j\mathbf{R}^i & 0 \\ 0 & \mathbf{F}_j^i\mathbf{R}^i & \mathbf{G}_j^i\mathbf{R}^i & \mathbf{A}^j \end{bmatrix} \begin{Bmatrix} \mathbf{x}^i \\ \mathbf{u'}_i^j \\ \mathbf{t'}_i^j \\ \mathbf{x}^j \end{Bmatrix}_{\tau+\Delta\tau} = \begin{Bmatrix} \mathbf{B}^i\mathbf{k}_{bc}^i + \mathbf{M}^i\mathbf{u}_{\alpha}^i + \mathbf{M}_i^j\mathbf{R}_i\mathbf{u'}_{\alpha i}^j \\ \mathbf{B}^j\mathbf{k}_{bc}^j + \mathbf{M}^j\mathbf{u}_{\alpha}^j + \mathbf{M}_j^i\mathbf{R}_i\mathbf{u'}_{\alpha i}^j \end{Bmatrix}_{\tau+\Delta\tau} , \tag{19}$$

where $\mathbf{A}^i$, $\mathbf{B}^i$ and $\mathbf{M}^i$ belong to the boundary of the ith grain; $\mathbf{A}^i$ and $\mathbf{B}^i$ are the blocks where the load conditions are applied. The blocks $\mathbf{F}_i^j$, $\mathbf{G}_i^j$ and $\mathbf{M}_i^j$ are the interfaces between the ith and jth grains. The $\mathbf{R}_i$ matrix represents the transformation from the global to the local coordinate system, assuming as a reference the local coordinates of the flat surface corresponding to the interface of the ith grain. The vector $\mathbf{x}^i$ represents all the traction and displacements unknowns to be evaluated in the elements corresponding to the boundaries and the vector $\mathbf{k}_{bc}^i$ are the known boundary conditions applied in the global coordinate system. At the interfaces, displacement $\mathbf{u'}_i^j$ and traction $\mathbf{t'}_i^j$ are directly evaluated in the local co-

ordinate reference. The last three displacement step responses are defined by $\mathbf{u}_{\alpha i}$, where $\mathbf{u}_{\alpha j}$ is for blocks belonging to the boundaries and $\mathbf{u'}^{j}_{\alpha i}$ the interfaces blocks in the local coordinates. All the transformations applied for the interface fields are very useful to assess contact or separation conditions in the failure analysis. Finally, the final matrix equation is

$$\mathcal{A}\mathcal{X}_{\tau+\Delta\tau} = \mathcal{F}_{\tau+\Delta\tau} \quad , \tag{20}$$

where $\mathcal{A}$ is the matrix of the overall system of equations and $\mathcal{X}_{\tau+\Delta\tau}$ is the unknown vector, both in the left-hand side of Eq. (19). The independent $\mathcal{F}_{\tau+\Delta\tau}$ vector is updated at every time step, as it contains all the known boundary conditions and the displacement information from the previous steps corresponding to the right-hand side of Eq. (19). Equation (20) computes the first mechanical response in terms of surface traction and displacement directly over the grain boundaries of the aggregate. Now, the surface stress and strain components are easily calculated by the Hooke's law, Cauchy's theorem and the parametric advantages provided by the BEM as extensively explained in [40]. In this case, the displacement $\mathbf{u'}^{j}_{i}$ and traction $\mathbf{t'}^{j}_{i}$ must be known in the global coordinate system using the inverted transformation matrix $\mathbf{R}_i^{-1}$. It results more convenient because the stiffness tensor $\mathbf{C'}_i$ can be used without any additional transformation. This formulation was successfully applied for quasi-static and transient regimes by Galvis [33] who also showed in detail the procedure for the discretization, integration and the required implementation steps to reproduce the micromechanical model of these heterogeneous materials.

3. Grain boundary model

The failure analysis of GBs in polycrystal aggregates has been the object of study through continuum, atomistic or multiscale approaches. The modeling of this failure condition requires a complex and detailed analysis in the interfaces that represent the transition region between two grains with distinct crystalline orientations. Hence, the atomistic modeling of GBs is presented using LAMMPS, where several GB configurations are analyzed using MD. As a validation, the evaluation of the GB energy (γ_{GB}) is evaluated as a function of the crystalline orientation angle for Fe with bcc lattice.

The importance of the study of the GBs from an atomistic view is to capture the effects on different GB properties such as segregation, diffusion, sliding and migration [41, 42]. Phenomena such as the formability and fracture behavior of polycrystalline materials are influenced by the presence of second phase precipitation at the grain boundaries [43]. Several works in the literature [44, 45] defined that, as the level of precipitation increases in the GBs, the fracture toughness and formability decrease affecting the overall behavior of the material with respect to the intergranular fracture. The GBs are formed during the grain growth and represent the discontinuity from the perfect crystal, being a region separating two grains of different phases. The orientations of these two grains differ from each other producing the grain boundary as a transition region, where the periodic character remains with a distinct atomic position compared to the grain interior [46]. Generally, the grain boundary is modeled as a bicrystal, Fig. 3(a). A mixed GB is defined by a specimen containing the crystals A and B with a random crystalline orientation, Fig. 3(b).

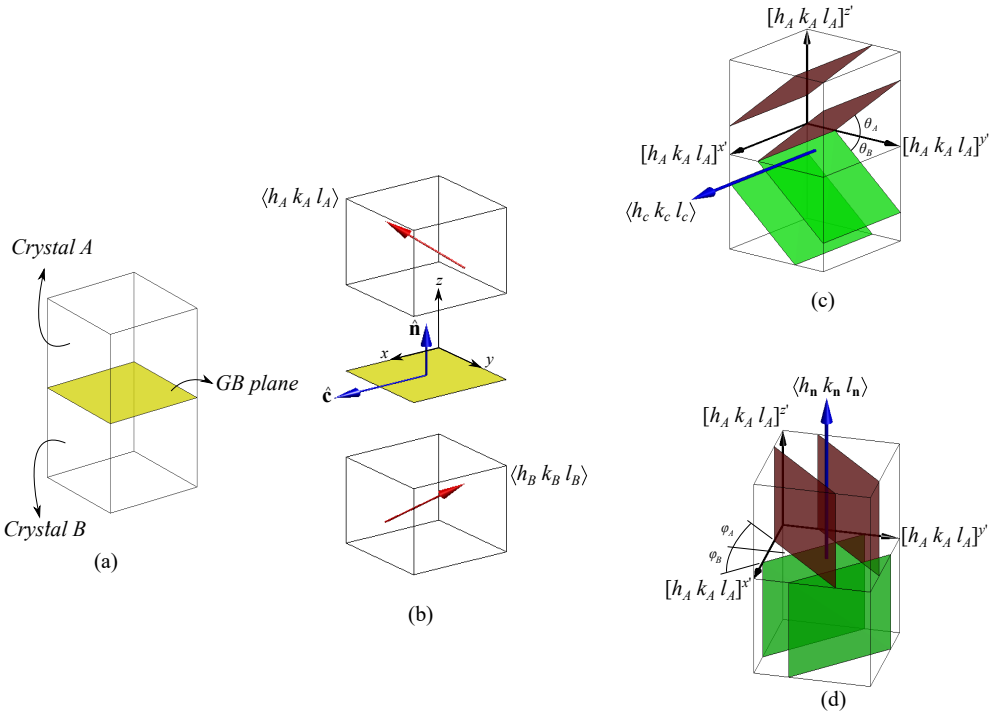

Figure 3: Bicrystal: (a) description, (b) mixed, (c) *tilt* and (d) *twist* GBs.

The GBs are fully characterized by the grain misorientation $\hat{\mathbf{c}} = \langle h_{\mathbf{c}} k_{\mathbf{c}} l_{\mathbf{c}} \rangle$ axis, which is identical in both grains. Over the $\hat{\mathbf{c}}$ axis, the *tilt* rotations θ_A and θ_B are defined in the crystals A and B respectively, Fig. 3(c). Additionally, the GB is also described by the normal $\hat{\mathbf{n}} = [h_{\mathbf{n}} k_{\mathbf{n}} l_{\mathbf{n}}]$ axis, Fig. 3(b). Over the $\hat{\mathbf{n}}$ axis, the *twist* rotations φ_A and φ_B are defined, Fig. 3(d). All these variables complete the five DOF needed for the description of the GBs, four of them from the $\hat{\mathbf{c}}$ and $\hat{\mathbf{n}}$ axes and one given by θ or φ. The GBs are classified into mixed, *tilt* and *twist* GBs, as presented in Fig. 3(c-d) [46].

The coincident-site lattice (CSL) is a geometrical model for the identification of different types of GBs. The GBs are divided into low-angle and high-angle interfaces. The low-angle GBs are considered as the interfaces with a misorientation

angle less than 15°. Several works reported low-angle GBs, such as Rouvierea et al. [47] that simulated *twist* interfaces from 0.5° to 12°. Also, Gao and Jin [48] used 3.4° *tilt* angle analysis of dislocation in Ni using MD simulations. Additionally, the energy of the low-angle GBs can be calculated through various analytical techniques presented in [49]. For both cases, low and high angle GBs, the atomic arrangement of the GB maintains its different periodic character from the atomic structure inside the grains. Therefore, the GB energy is considered higher than the energy in the crystal interior.

The CSL contemplates that the grain boundary energy is low when the coincidence of atomic positions in both adjacent grains is high because the number of bonds that are broken across the boundary is small [50]. Other definitions consider that the state of the minimum energy occurs when the atomistic arrangement is perfect without any discontinuity, the grain boundary energy is low when more atoms coincide with the positions of the perfect crystal than in a non-coincident state. The number of coincident-sites is determined by the simple superposition of the two crystals where some atoms will coincide, this process can represent a difficult task. In the literature, the GBs are identified by the reciprocal value (Σ) of the density of coincidence sites that is important to characterize the CSL. An extended explanation of how to evaluate the Σ parameter is presented by Lejcek [46]. At the first instance, the Σ values will be higher for low angle GBs.

In the MD simulation of GB energy, the bicrystal model considers periodic boundary conditions to avoid border effects. Depending on the misorientation angle of each grain, the final bicrystal structure must guarantee the exact periodicity

in the x, y and z axes. In this work, the CSL bicrystal is built using the *GBstudio*[1]. This is a software developed by Ogawa [51] for generating atomic coordinates in periodic GB models composed by two crystals. Hence, using *GBstudio* a set of symmetric *tilt* (STGB), anti-symmetric *tilt* (ATGB), symmetric *twist* and anti-symmetric *twist* grain boundaries are generated, see the details of these definitions in [46]. The input parameters are the lattice of the crystal structure, the mentioned five DOF of the bicrystal and the number of rotated unit cells along each axis. An illustration of a generated GB is shown in Fig. 4, this structure represents an example of an STGB bicrystal for a cubic bcc Fe.

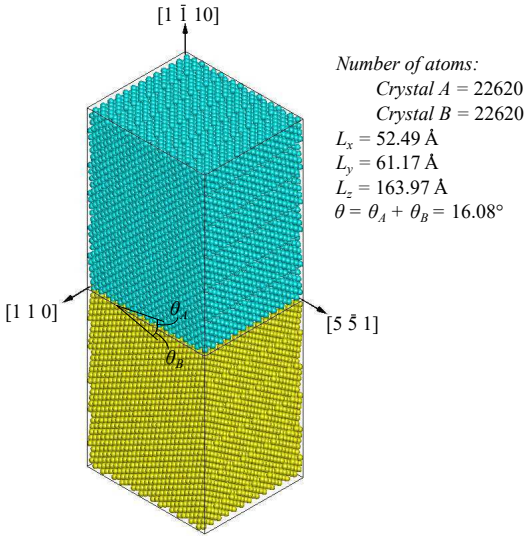

Figure 4: Bicrystal structure of a STGB $\Sigma 51\{1\,\bar{1}\,10\}$ in the $\langle 110\rangle$ direction.

In the STGB $\Sigma 51\{1\,\bar{1}\,10\}$ depicted in Fig. 4, the new axes of coordinates are $x = [110]$, $y = [5\bar{5}1]$ and $z = [1\,\bar{1}\,10]$. In this GB, the misorientation angles are the same as $\theta_A = 8.04°$ and $\theta_B = 8.04°$. The normal vector of the GB plane is

[1] https://staff.aist.go.jp/h.ogawa/GBstudio/indexE.html

the same as z, $\hat{\mathbf{n}} = [1\ \bar{1}\ 10]$. After the application of the misorientation angles in both crystals, the resulting new unit cell has a modified lattice size to guarantee the periodicity. In this case, the size of the resulting unit cell is $a_x = 4.04$ Å, $a_y = 2.039$ Å and $a_z = 0.283$ Å. Hence, denoting by N_x, N_y and N_z the number the unit cell is multiplied in each axis, in the example presented in Fig. 4, the unit cell is repeated by $N_x = 13$, $N_y = 3$ and $N_z = 29$ for each crystal. More details of the STGB $\Sigma 51\{1\ \bar{1}\ 10\}$ are presented in Fig. 5. A section is selected from the bicrystal, Fig. 5(a), where the perfect periodicity in the x- and y-axes is shown. The final crystalline structure is composed by two layers repeated along the $[5\bar{5}1]$ axis, Fig. 5(b) and shown in detail in Fig. 5(c) from the standard cubic bcc unit cell of Fe.

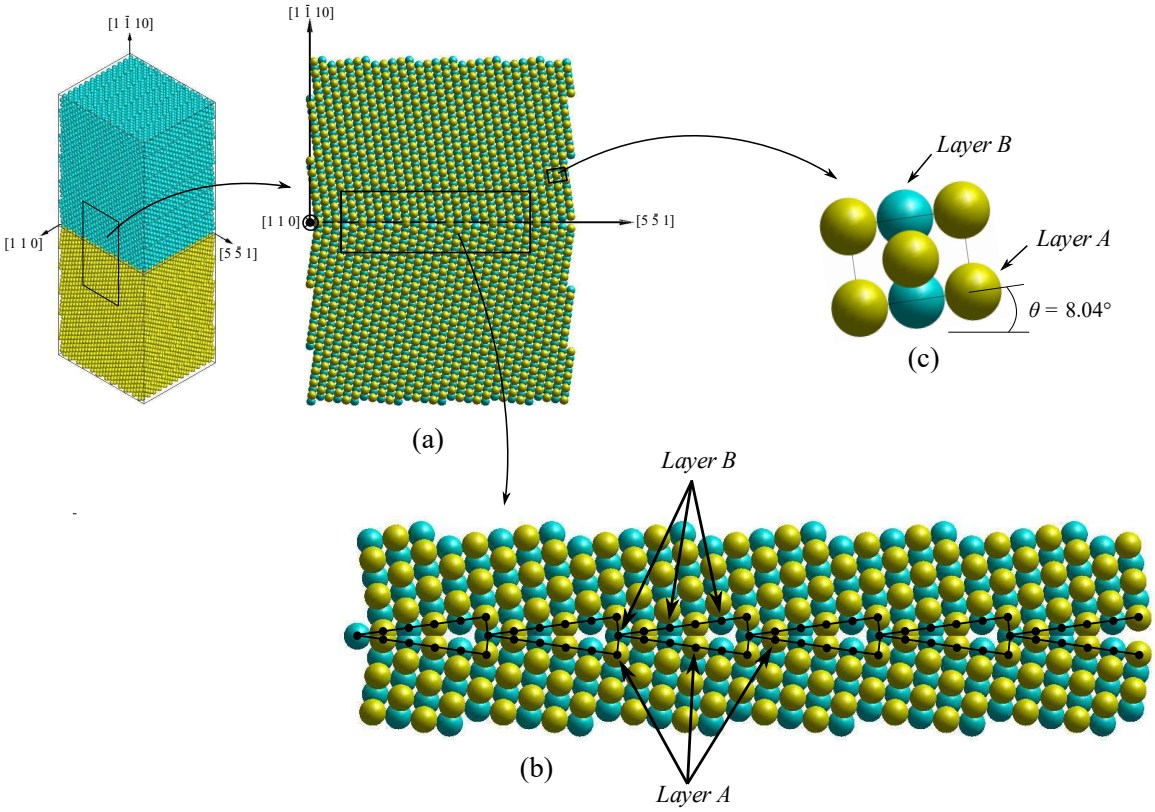

Figure 5: Detailed description of the STGB $\Sigma 51\{1\,\bar{1}\,10\}$ bicrystal.

The computational cell must be large enough to prevent interaction between the parallel boundaries and other finite-size effects [52]. In this work, the size of the bicrystal with dimensions L_x, L_y and L_z is considered as suggested by Sangid et al. [53] as $L_x, Ly \geq 5$ nm, and $L_z \geq 8$ nm. Owing to the periodicity, the structure is repeated and perfectly matched over the three axes.

In the literature, many studies have been carried out to identify the predominant type of GBs presented in metals and ceramics. It is known that interfaces with high coincident site density or low values of Σ are energetically favorable and frequently found in existing materials, commonly presented in asymmetrical

GBs [51, 54]. Extensive analyses over a large amount of GBs for different materials were presented by Watanabe et al. [55]. They studied the type and frequency of GBs in a rapidly solidified and annealed Fe-6.5 mass%Si alloy, high frequencies of low-angle boundaries and coincident boundaries were observed with $\Sigma 3$, $\Sigma 9$, $\Sigma 11$, $\Sigma 17$ and $\Sigma 19$ in the $\langle 110 \rangle$ rotation axis. Using the same alloy, some additional studies to control the grain character distribution and its effects on the deformation using directional recrystallization were presented by Zhang et al. [56]. The authors reproduced elongated grain structures, high frequency of both low angle and low Σ values. An analysis in hot-rolled Fe-6.5 mass%Si was carried out by Zhang et al. [57]. They investigated the effects of annealing on GB texture evolution. Their results were also compatible with the last two references, as the authors obtained a large percentage of $\Sigma 3$, $\Sigma 9$, $\Sigma 13$ and $\Sigma 27$. At 800°C annealing temperature, the mean frequencies of misorientation angles were for 5° and 30°. In the case of 650°C annealing temperature, the higher frequencies found were from 0° to 30°. From the conclusions presented by the mentioned publications, it is feasible to consider a large number of STGB, ATGB, STwGB, and ATwGB to statistically characterize a representative quantity of interfaces presented in a polycrystalline Fe material, in order to derive an intergranular failure criterion from the atomistic scale to be applied in the mesoscale.

Molecular dynamic simulations using LAMMPS are carried out to evaluate the GB energy on Fe of a set of STGBs and STwGBs, for a *tilt* angle varying from 0° to 180° and *twist* angle varying from 0° to 60°. The GB structures are built with the *GBstudio* using the lattice parameter a and according to the mentioned box size requirements. The STGBs and STwGBs structures are listed in the supplementary material item B. First, full periodic boundary conditions are

imposed to the GB in the x, y and z axes. Next, using the EAM [58] potential, the constitutive Fe material is adequately modeled. Finally, the energy minimization to reach the structural relaxation and stable equilibrium of the atomistic system is attained. Owing to the dependency of the potential energy on the atomic positions, the imperfections in the structure configuration can cause specific atomic positions where the evaluation of the potential energy results in very high values. The most common method used for energy minimization of atomistic systems is the conjugate gradient (CG), due to its efficiency to convergence.

In the minimization of the GB energy, the system is previously annealed to 800 K and then quenched to 10 K [53]. Thermal fluctuations allow to overcome energy barriers between the local minima to reach a better structural relaxation. From an initial temperature T_i and using the time step $dt = 1$ fs, the system is stabilized during 1 ps at T_i, keeping the volume of the simulation box fixed. The pressure remains constant at 0 bar in the whole thermal process. Thus, the annealing and quenching procedures begin: i) the temperature is increased from T_i to 800 K, ii) the temperature is steady at 800 K, iii) the temperature is reduced to 10 K, iv) the temperature is steady at 10 K. This thermal process is achieved using the *NPT* ensemble which allows the control of the temperature and pressure through the integration over time. The *NPT* is implemented in LAMMPS based on the Nose-Hoover isothermal-isobaric style presented by Tuckerman et al. [59]. Each process is simulated during 10 ps. At this stage, the structure is ready to be relaxed using the CG method. In the process of potential energy minimization, the volume of the box may oscillate slightly due to the readjustment in the atomic positions, especially in the normal GB direction. Then, in a second minimization process, it is guaranteed that there is no residual pressure, forcing a zero external pressure

during the minimization process in this direction. The completed algorithm is shown in Fig. 6, it represents the LAMMPS script implemented in this work, see the supplementary material item B. The evaluation of the GB energy is quite similar to the methodology used in [60, 61].

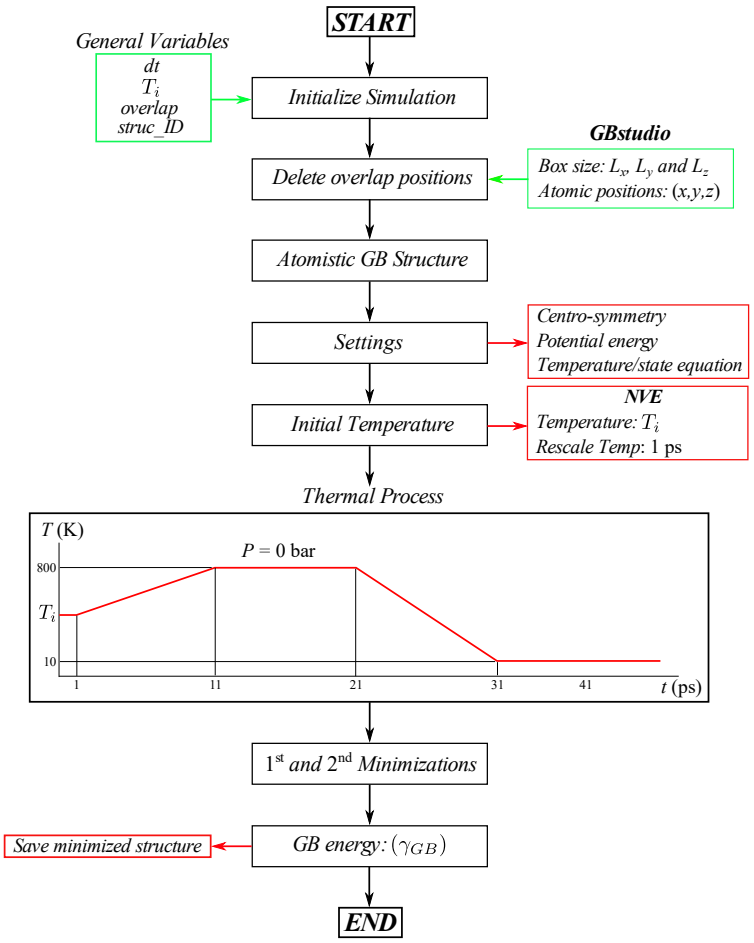

Figure 6: Algorithm to evaluate the GB energy using LAMMPS.

The GB energy is calculated comparing the final energy obtained by the simulation $E_{Bicrystal}$ and the energy of a perfect crystal with the same number of atoms

E_{perfect} as follows

$$\gamma_{\text{GB}} = \frac{E_{Bicrystal} - E_{\text{perfect}}}{2(L_x L_y)} \quad , \tag{21}$$

where $A = L_x L_y$ is the GB area, the factor of two, is because the system contains two interfaces owing to the periodic boundary conditions in the z-axis. The corresponding energy to a perfect crystal is computed as $E_{\text{perfect}} = NE_c$, where E_c is the cohesive energy and N the total number of atoms in the system. An initial energy minimization of a unit cell was performed to obtain the correct lattice parameter a and the cohesive energy E_c corresponding to the EAM model.

In the bicrystal construction, the resulting GB plane is composed by a periodic atomistic arrangement with distinct crystalline orientation compared with the grain interior. This special arrangement in the interface can produce overlap atomic sites, where the distance between atoms is less than the equilibrium lattice parameter a. The overlap effect produces very high values of the potential energy and in the interatomic force calculations. Therefore, there are two variables to be fitted to obtain a better local minimum energy value, the initial temperature T_i and *overlap*, as shown in the LAMMPS script in the supplementary material B. By fitting the *overlap* parameter, the atomic sites that cause the superposition effects are deleted. When the GB contour is defined, there are two groups of atoms corresponding to each grain with the same crystalline structure, although with different orientations. This concept is depicted in Fig. 4, where the upper grain is given in blue and the lower in yellow, and their orientations being defined by θ_A and θ_B. After overlaying these grains, also certain atoms of both groups overlap. Then, these atoms must be removed from one group. In this way, the parameter *overlap* is defined so that when the distance between a pair of atoms of different groups is

less than the *overlap* value, the atom of the first group is eliminated. In this work, *overlap* values were defined for more than 20% of the atomic radius. According to the maximum temperature defined in the thermal process and the lattice parameter a, the selected intervals to evaluate the GB energy as a function of these two variables are defined in Table 1.

Variable	*Interval*
T_i (K)	10 – 650
overlap (Å)	1.5 – 2.70

Table 1: Variables to be fitted.

The temperature interval is divided into 10 values and the *overlap* interval into 8. In total, this results in 80 simulations for each bicrystal: i) the *tilt* low angle GB $\Sigma 99\{1\,\bar{1}\,14\}$ with $\theta = 11.59°$ in the direction $\langle 110\rangle$, and ii) the *twist* low angle $\Sigma 91\{10\,\bar{1}\,\bar{9}\}$ with $\varphi = 10.4°$ in the rotation axis $\langle 111\rangle$. For the *tilt* case, the structure has $41,184$ atoms and in case of *twist* $54,208$ atoms. The *tilt* results are presented in Fig. 7. For a small value of overlap, the GB energy is high in the whole temperature interval. It is gradually decreasing when the *overlap* increase, the minimum GB energy is $942.42\,\mathrm{mJ/m^2}$ at a temperature $T_i = 142.92\,\mathrm{K}$ and *overlap* of 2.58 Å.

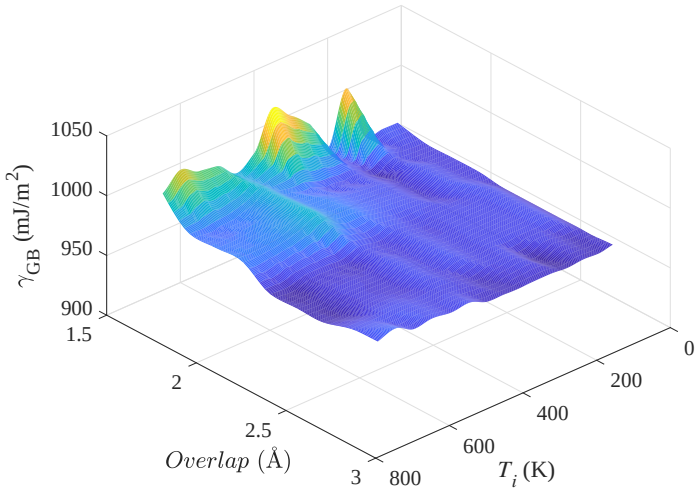

Figure 7: GB energy of the *tilt* $\Sigma 99\{1\,\bar{1}\,14\}$ in terms the initial temperature and the overlap parameters.

535 In the case of *twist*, results are presented in Fig. 8. There is a uniform behavior of high GB energy values for the whole temperature interval with the overlap between 2 Å and 2.5 Å. The minimum GB energy is $907.79\,\mathrm{mJ/m^2}$, at a temperature $T_i = 526.92\,\mathrm{K}$ and *overlap* of 2.01 Å.

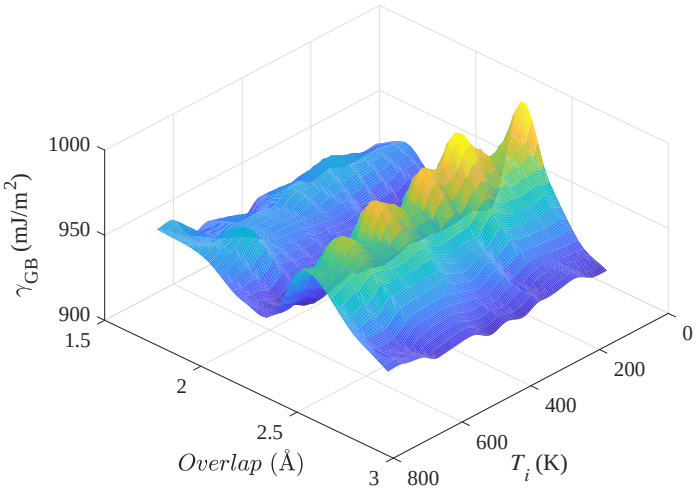

Figure 8: GB energy of the *twist* $\Sigma 91\{10\,\bar{1}\,\bar{9}\}$ in terms the initial temperature and the overlap parameters.

Using the fitted values, the GB energy is evaluated for a set of STGBs and STwGBs where the maximum, mean and minimum number of atoms are presented in Table 2.

	tilt	*twist*
Max	61,776	74,256
Mean	43,589	50,055
Min	27,872	31,824

Table 2: Number of atoms used to model the STGBs and STwGBs, from the structures presented in supplementary material item B.

The GB energy given in terms of the *tilt* angle θ is shown in Fig. 9, these results are compared to the values presented by Tschopp et al. [62] using the same EAM

potential. Results show to be close to the reference values, especially for misori-
545 entation angles greater than 60°. Furthermore, two deep values are identified for $\Sigma 3(1\bar{1}2)$ and $\Sigma 11(3\bar{3}2)$. Additionally, it can be observed the strong variation of the GB energy depending on the misorientation angle.

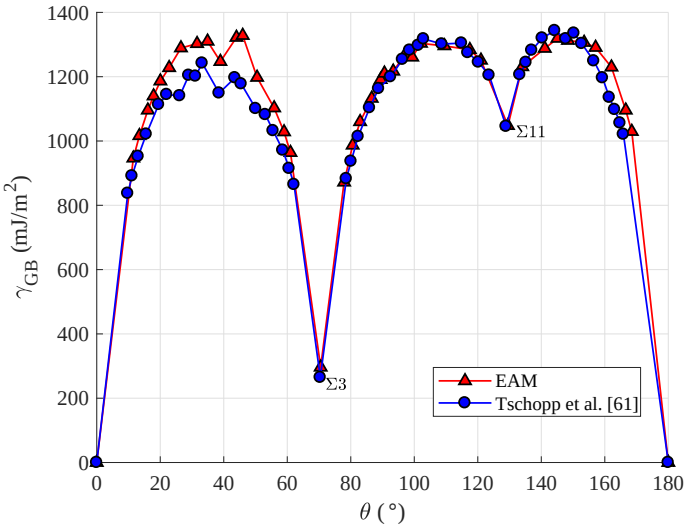

Figure 9: GB energy γ_{GB} of STGBs ⟨110⟩ in terms of the *tilt* angle θ.

The results for the *twist* case are shown in Fig. 10. Comparisons are carried out with the values given by Wolf [54] and Runnels [63]. They used different
550 approaches for the analysis, Wolf [54] used an iterative minimization algorithm with a Johnson-type pair potential. Runnels [63] proposed a relaxation method using the EAM and Lennard-Jones potentials.

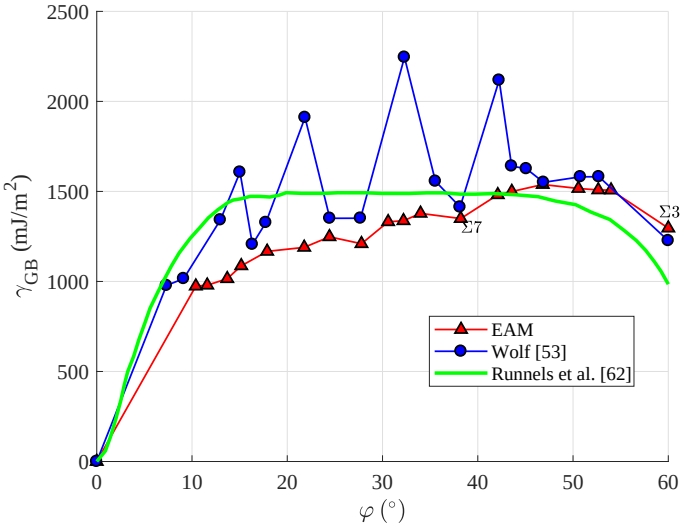

Figure 10: GB energy of STwGBs ⟨111⟩ in terms of the *twist* angle φ.

A steadier behavior of the GB energy was obtained compared to the two references in Fig. 10. In this case, there are no deep characteristic values, that means the STwGB structures contain large defects from the perfect crystal. Even for low values of the reciprocal density $\Sigma 3$ and $\Sigma 7$, the CSL fails from its basic definition. The GB energies evaluated from the STwGBs result in higher values compared with the evaluated from the STGBs. Otherwise, the values of the misorientation angle of the STwGB show to be more regular than the GB energy for STGB.

4. Multiscale failure

After the GB energy evaluation, the MD algorithms to obtain the stress-strain behavior of each GB under tensile and shear modes are shown. The multiscale bridging is carried out applying the asymptotic scaling analysis to these stress-strain curves for computing the critical energy densities at the mesoscale. The

failure condition is analyzed using the generalized energy failure criterion, considering the variation of the lattice structure in each GB. Finally, under dynamic boundary conditions, the propagation of integranular failure cracks though the polycrystalline structure was simulated.

4.1. Critical energy densities

Molecular dynamics simulations using LAMMPS are carried out to evaluate the cleavage and shear failure of the minimized Fe GB structures. The important fact in these simulations is to capture the variation of the critical cleavage E_{nc} and shear E_{sc} energy densities depending on the GB orientations. This atomistic model offers a more realistic behavior of the failure process at the interfaces, taking into account the brittle and ductile levels of each GB. For this purpose, a set of 101 containing STGB, ATGB, STwGB, and ATwGB is generated varying the reciprocal of the density coincident-sites from $\Sigma 3$ to $\Sigma 81$, see the supplementary material item C. The bicrystal contains an initial central crack to get a more brittle failure and also to reduce the plastic deformation regime. Also, a central crack gives the possibility for simulating shear failure in the positive and negative direction for each axis. The dimensional specifications are shown in Fig. 11. This configuration is similar to the model used by Dingreville et al. [64] and in references [65, 66].

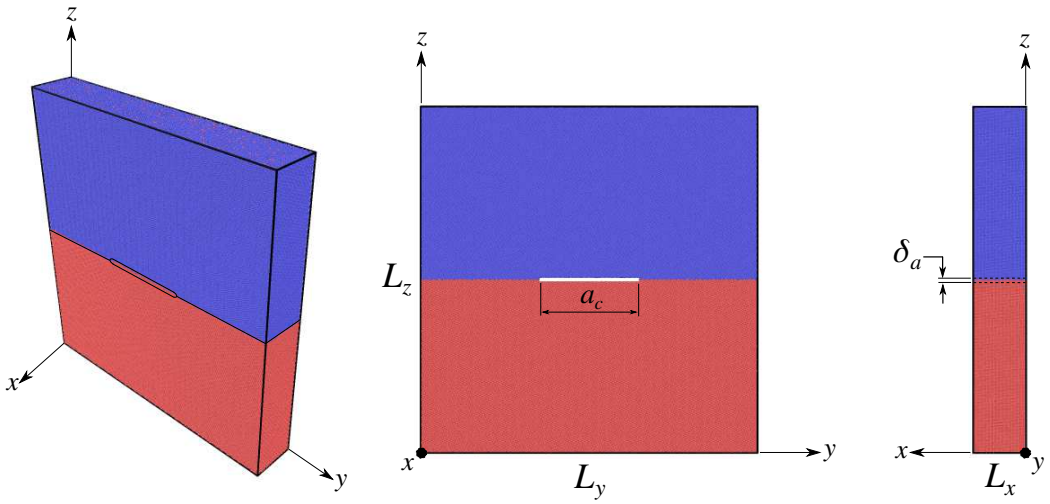

Figure 11: Nanoscale specimen for failure simulations.

In Fig. 11, a_c is defined as $0.3L_y$ and δ_a is equal to $3a$, a being the lattice parameter. This is to avoid the interaction between atoms in the crack surfaces during the energy minimization process. Furthermore, $L_x/L_y < 1$ being L_x large enough to avoid interference on the surface effect produced by the periodic boundary conditions between the walls at $x = 0$ and $x = L_x$. Statistical information such as the number of atoms, dimensional details and the GB energies of the nanoscale specimens are presented in Table 3.

	Atoms	L_x	L_y	L_z	γ_{GB}
Max	2,754,000	74.18	755.09	758.44	3,288.40
Mean	623,367	25.42	541.62	541.43	1,478.62
Min	199,680	10.68	346.91	377.67	781.96

Table 3: Details of the nanoscale specimens, GB energy γ_{GB} expressed in (mJ/m^2) and length values in (Å).

It can be observed in Table 3 that there is a variation in the specimen size from 199,680 to 2,754,000 atoms. This is due to the minimum size of a unit GB cell defined by the *GBstudio* package, that guarantees the perfect periodicity in the x, y and z-axes. In addition, the GB energy γ_{GB} gives an idea of the defect fluctuation caused by the misorientation. The transition lattice structure requires the consideration of the shear analysis in both x and y-axes and also in the positive and negative directions. Then, in total, five simulations are run for each bicrystal, one for cleavage and four for shear loads. In the case of shear in the x-direction, the initial crack is fitted on the x-axis and $L_x/L_y > 1$. Dynamic boundary conditions are applied through a deformation rate $\dot{\varepsilon}$ using the definitions in Table 4.

	$z = 0$	$z = L_z$
Tensile (n)	$\dot{\varepsilon}_{zz}$	$-\dot{\varepsilon}_{zz}$
Shear $(xz^{\pm})$	$\pm\dot{\varepsilon}_{xz}$	$\mp\dot{\varepsilon}_{xz}$
Shear $(yz^{\pm})$	$\pm\dot{\varepsilon}_{yz}$	$\mp\dot{\varepsilon}_{xz}$

Table 4: Dynamic boundary conditions for cleavage and shear tests.

A high deformation rate is applied to the GB after the energy minimization process, where the structure is kept at a temperature of 10 K. First, the initial variables are defined, the time step $dt = 1$ fs, the temperature T is 296 K and the deformation rate $\dot{\varepsilon}$ is equal to 10^9/s and 10^{10}/s for cleavage and shear analyses, respectively. Before the application of the deformation rate, the temperature is increased from 10 K to 296 K allowing the box to contract or expand in all directions during 10 ps within an independent zero pressure in each axis of the coordinate system. This process is achieved by applying a Langevin thermostat [67] and a

Parrinello-Rahman-type barostat, on an isobaric-isothermal (*NPT*) ensemble [68–70]. This initial part of the algorithm is common for both tensile and shear loads as illustrated by the flowchart shown in Fig. 12.

In order to impose the tensile load, the z expansion is applied on the box, rescaling uniformly at each time step, under controlled conditions of strain rate using the fix deform command. The transverse directions allow contractions maintaining $P_x = P_y = 0$ in order to simulate the Poisson effect. It is carried out through a $NL_zP_xP_yT$ ensemble, similar to other investigations of mechanical deformation with MD [71, 72]. In the case of shear deformation, e.g. ($yz^{\pm}$), the boundary conditions must be changed on the y and z-axes to non-periodic conditions, while the x is kept as periodic. The deformation is imposed using the *velocity* command. Notice that this process is developed at a constant temperature of 296 K, and it is calculated using the total kinetic energy of the group of atoms. Hence, the temperature must be computed partially after excluding the y-component. These procedures are depicted inside the dashed region in Fig. 12 and the detailed LAMMPS scripts are presented separately in supplementary material item C.

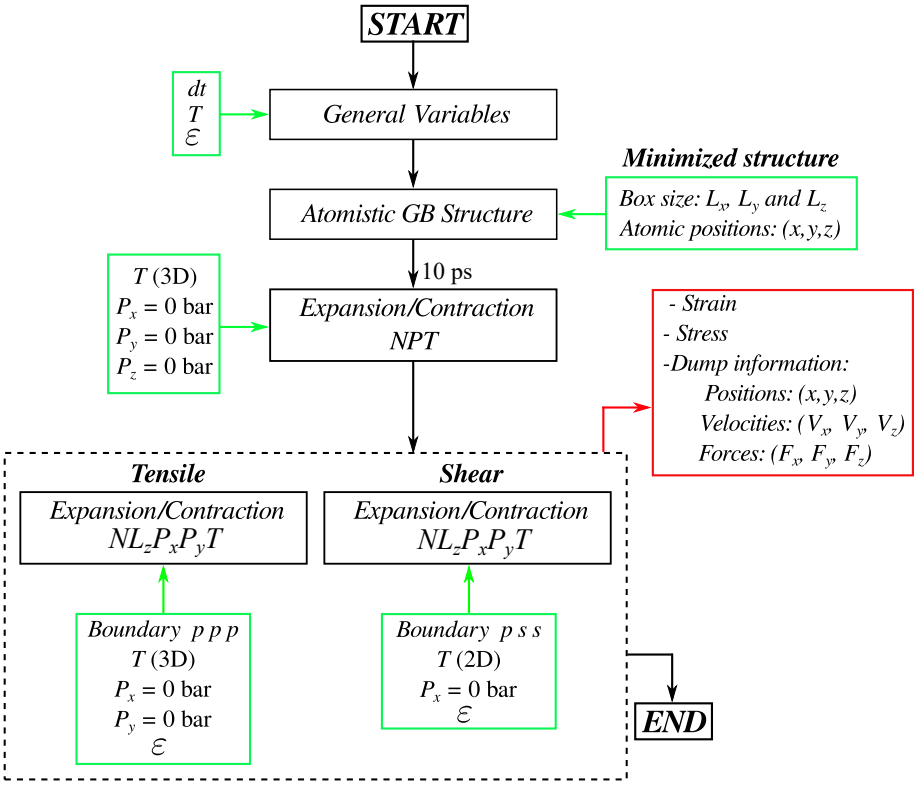

Figure 12: Algorithms for cleavage and shear failures tests using LAMMPS.

625 The results of these MD models are shown in Fig. 13, for five GB structures under cleavage (n) and shear (yz^+) loading cases. The variation in the stress-strain GB behavior and mechanical properties such as the maximum stress and ultimate strength of these GBs can be appreciated. These curves are expressed by the Virial stress definition of the macrostate and the applied strain rate to the GB box.

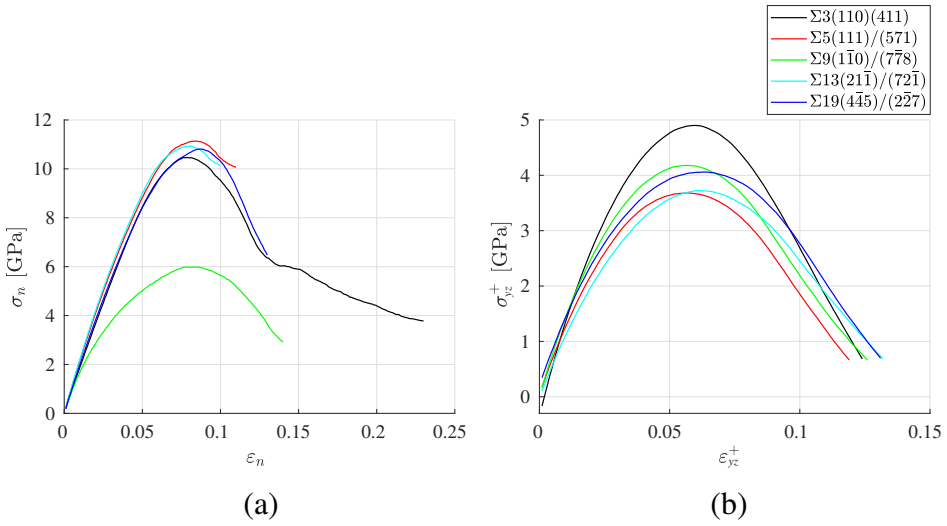

Figure 13: Stress-strain GB curves for five configurations: (a) cleavage and (b) shear.

In Table 5, the numerical values of the maximum stress and GB energy for each GB is given for both cases presented in Fig. 13. In the $\Sigma 5$, $\Sigma 9$, $\Sigma 13$, and $\Sigma 19$ structures, ductile failure is predominant under shear load. The opposite situation appears under tensile load for $\Sigma 3$, where a high deformation level is required to fail. Hence, from the energetical point of view, some conclusions could be defined. According to the CSL model, the $\Sigma 3(1\,1\,0)/(4\,1\,1)$ structure is closest to a perfect GB, owing to the high number of coincident sites that means its energy is at the lowest value as $1,160.90\,\mathrm{mJ/m^2}$. This concept can fail sometimes, due to the geometrical character of the CSL model. An explanation can be made analyzing the *tilt* angle θ, e.g. between the $\Sigma 3\{1\,\bar{1}\,2\}$ and $\Sigma 3\{1\,1\,1\}$ structures, which are $70.52°$ and $109.5°$ respectively. Even though these structures have the same number of coincident sites $\Sigma 3$, the $\Sigma 3\{1\,1\,1\}$ GB has more defects concerning the perfect structure. Moreover, the $\Sigma 3\{1\,\bar{1}\,2\}$ represents a low energy value according to the behavior presented in Fig. 9.

GB structure	σ_n^{max}	σ_{yz}^{+max}	γ_{GB}
$\Sigma 3(1\,1\,0)/(4\,1\,1)$	10.46	4.90	1,160.90
$\Sigma 5(1\,1\,1)/(5\,7\,1)$	11.13	3.68	1,377.61
$\Sigma 9(1\,\bar{1}\,0)/(7\,\bar{7}\,8)$	5.98	4.17	3,163.04
$\Sigma 13(2\,1\,\bar{1})/(7\,2\,\bar{1})$	10.93	3.72	1,267.35
$\Sigma 19(4\,\bar{4}\,5)/(2\,\bar{2}\,7)$	10.81	4.05	1,381.11

Table 5: Critical stress values expressed in (GPa) and GB energy in (mJ/m^2).

Considering the last definitions, it is worth noting that the $\Sigma 9(1\,\bar{1}\,0)/(7\,\bar{7}\,8)$ structure has the highest GB energy of $3,163.04\,mJ/m^2$. This fact reflects more probability to fail especially under tensile load. The results also show the difference in the stress level between the models as expected. The nucleation of defects such as dislocations caused by the shear load could lead the slip failure mechanisms to be more susceptible to fail. A complete analysis of the relationship between cleavage and shear modes in grain boundaries was presented by Paliwal and Cherkaoui [73]. They found a drastic increment on the maximum shear stress caused by the application of boundary conditions defined by $0° < \theta < 85°$ being $\theta = \arctan\left(\dot{\varepsilon}_{zz}/\dot{\varepsilon}_{yz}\right)$, contrary to the tensile stress that presents a slower variation in its magnitude. Finally, some cases of cleavage and shear failure are presented in Fig. 14, on the $\Sigma 37(2\,\bar{2}\,\bar{1})/(2\,\bar{2}\,1)$ structure with 1,417,248 atoms. In this figure, the blue color represents the bcc structures and the red color, the transition lattices in the interfaces. In the left figures, the 3D model is depicted. The central and right figures show the separation process.

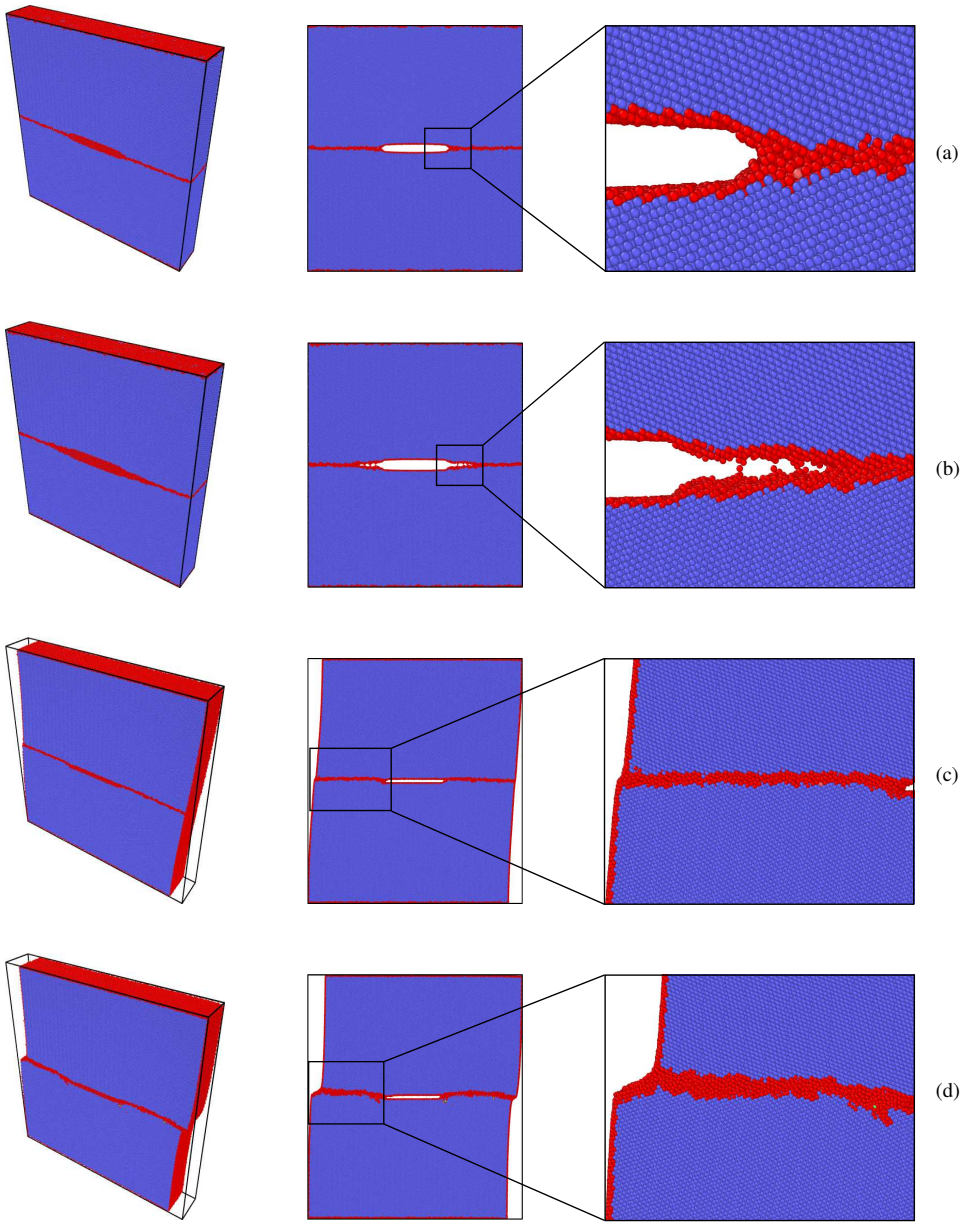

Figure 14: $\Sigma 37(2\bar{2}\bar{1})/(2\bar{2}1)$ structure, cleavage failure: (a) $t = 50\,\text{ps}$, $\sigma_n = 9.28\,\text{GPa}$, $\varepsilon_n = 5\%$ and (b) $t = 70\,\text{ps}$, $\sigma_n = 10.26\,\text{GPa}$, $\varepsilon_n = 7\%$; shear failure: (c) $t = 50\,\text{ps}$, $\sigma_{yz}^{+} = 3.38\,\text{GPa}$, $\varepsilon_{yz}^{+} = 5\%$ and (d) $t = 80\,\text{ps}$, $\sigma_{yz}^{+} = 1.31\,\text{GPa}$, $\varepsilon_{yz}^{+} = 9\%$.

These results present the failure under different modes. Owing to the inclusion of the initial crack, it can be inferred that the separation of the effective GB area is easy to be captured. As mentioned, the trend for both models is to fail on the interface GB plane, with the shear stress being approximately 30% of the tensile stress.

4.2. Asymptotic scaling

The material behavior presents an increment in its mechanical stress when the specimen size tends to be small, also in case of imposition of high deformation rate. This effect can be observed in the results shown in Fig. 13, where the level of the yield strength reaches up to 11 GPa approximately in the nanoscale under tensile strain. This is evidently much higher than the well-known strength values in microscopic scales of MPa order. Hence, the scaling effects represent a challenge in the multiscale modeling where several approximations have been developed to attempt the scaling of mechanical properties such as yield and rupture limits. Some numerical models were treated before and can be found in the literature such as in [19, 23, 24]. In these investigations, several efforts were presented, in order to find functions to represent the scaling change in terms of size and deformation rate for pure metals like copper. More related to the work presented here, Hammami and Kulkarni [20] showed the rate dependence of grain boundary sliding via atomistic simulations.

Due to the number of GBs considered in this approach, and the interval of atoms used in their construction, Table 3, it would take a large processing time for simulating both the length and rate dependencies. Hence, as a first approximation, it is proposed to adopt the asymptotic scaling analysis presented by Chen et al. [24] applied for different size length of geometrically similar structures.

They proposed a simple formulation that could represent the size effect on the strength, based on the asymptotic relationship between the nominal strength and sizes widely exposed before in [22]. Then, Eq. (22) is applied to scale the stress between the nominal parameters, such as $\sigma_{\mathfrak{na}}$ that correspond to the average of the maximum stress of all GBs, and $\sigma_{\mathfrak{m}}$ being the stress at microscale.

$$\begin{cases} \sigma_{\mathfrak{o}} = \sigma_{\mathfrak{na}} & \mathcal{D} \leq \mathcal{D}_{\mathfrak{na}} \\ \log\sigma_{\mathfrak{o}} = \log\sigma_{\mathfrak{m}} + (\log\sigma_{\mathfrak{na}} - \log\sigma_{\mathfrak{m}})\cdot & \\ \qquad \left[1 - \sin\left(\frac{\pi}{2}\frac{\log\mathcal{D} - \log\mathcal{D}_{\mathfrak{na}}}{\log\mathcal{D}_{\mathfrak{m}} - \log\mathcal{D}_{\mathfrak{na}}}\right)\right] & \mathcal{D}_{\mathfrak{na}} < \mathcal{D} < \mathcal{D}_{\mathfrak{m}} \\ \sigma_{\mathfrak{o}} = \sigma_{\mathfrak{m}} & \mathcal{D}_{\mathfrak{m}} \leq \mathcal{D} \end{cases} . \tag{22}$$

The variables to be found are $\sigma_{\mathfrak{o}}$ that is the nominal stress for cleavage and shear failure at the desired length size $\mathcal{D}$. In this procedure, the entire stress-strain curves obtained from the MD simulations are scaled. The $D_{\mathfrak{na}}$ term is considered as the nanoscale size, in which any smaller size $\mathcal{D} \leq \mathcal{D}_{\mathfrak{na}}$ produces a constant strength $\sigma_{\mathfrak{o}} = \sigma_{\mathfrak{na}}$. The opposite effect is considered if $\mathcal{D}_{\mathfrak{m}} \leq \mathcal{D}$ being $\mathcal{D}_{\mathfrak{m}}$ the microscale size limit. Some assumptions have been taken due to the lack of experimental data from these scales. As indicated by Bazant [74], the characteristic dimension $\mathcal{D}_{\mathfrak{na}}$ can be chosen arbitrarily. Hence, if the characteristic size of each GB is defined by the average of the GB plane, the $\mathcal{D}_{\mathfrak{na}}$ term can be evaluated by the average dimension over all 101 GBs planes as follows

$$\mathcal{D}_{\mathfrak{na}} = \frac{1}{N_{GB}}\sum_{k=1}^{N}\frac{L_x^{\mathfrak{na},k} + L_y^{\mathfrak{na},k}}{2}, \quad \begin{cases} L_x^{\mathfrak{na}} = L_x & \rightarrow \quad shear\,(xz^{\pm})\,mode \\ L_y^{\mathfrak{na}} = L_y & \rightarrow \quad shear\,(yz^{\pm})\,mode \end{cases} , \tag{23}$$

where N_{GB} is the number of GBs. As mentioned before, there are two defined specimens according to the $xz^{\pm}$ or $yz^{\pm}$ shear tests, in which $L_x/L_y < 1$ and $L_x/L_y >$

1 are satisfied, respectively. Note in Eq. (23) that $\mathcal{D}_{\mathrm{na}}$ takes into account the main lengths used in the shear failure. The σ_{na} limit remains constant if $\mathcal{D} \leq \mathcal{D}_{\mathrm{na}}$ and, according to this hypothesis, it is possible to evaluate σ_{na} as the average of the maximum stress over all GBs, depending on the failure test. In conclusion, the nanoscale limits $(\mathcal{D}_{\mathrm{na}}, \sigma_{\mathrm{na}})$ reflect an approximation of an average material that can represent the assembly of all nanoscale GBs.

For the definition of the macroscopic limits $(\mathcal{D}_{\mathrm{m}}, \sigma_{\mathrm{m}})$, the stress value is taken from the investigation presented by Sakui and Sakai [75]. They studied the effect of strain rate, temperature and grain size on the lower yield stress and flow stress of polycrystalline pure iron. Then, for a $10.3\,\mu$m grain size at 290 K under 10^0/s of deformation rate, they found a lower yield stress of 490 MPa. The size length was not reported by the authors but, in accordance with the grain size, the macroscopic length limit is assumed as $100\,\mu$m. Ideally, with this value, the microscopic polycrystalline structure will contain about $1,000$ grains, which is enough to guarantee the convergence for elastic and mechanical properties. Now, the asymptotic limits were defined, the scaling procedure can be applied to the stress curves over all previous results of nanoscale failure. Defining the desired transitional scale size $\mathcal{D}$ equal to $1\,\mu$m, this value approximately corresponds to the average length of all boundary elements used in the discretization of the polycrystal aggregate. In summary, the required scaling values for the tensile test are shown in Table 6.

$\mathcal{D}_{\mathrm{na}}$	σ_{na}	$\mathcal{D}$	$\mathcal{D}_{\mathrm{m}}$	σ_{m}
0.0529	10.90	1	100	0.490

Table 6: Limit scaling values for tensile test, length expressed in (μm) and stress in (GPa).

Thus, the complete set of cleavage critical energy density E_{nc} is presented in Fig. 15. These values are obtained from the area under the stress-strain scaled curves.

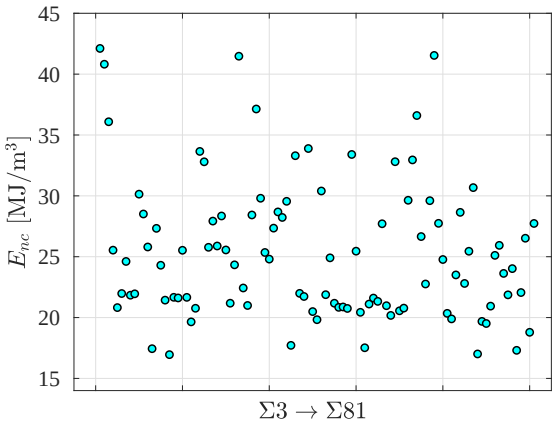

Figure 15: Critical cleavage E_{nc} energy density depending on the GB structure.

The maximum critical cleavage energy density is $42.11\,\mathrm{MJ/m^3}$ and the minimum is $16\,\mathrm{MJ/m^3}$. From Fig 15, it is observed that E_{nc} lies between these two limits, presenting a scattered behavior. For the shear cases, the only difference is the microscopic stress limit. Defining the shear stress limit at the nanoscale ($\sigma_{\mathfrak{na}_s}$), being the average over all the maximum shear stress found in the 101 GBs, and defining the ratio $\eta = \sigma_{\mathfrak{na}_s}/\sigma_{\mathfrak{na}}$ expressed by

$$\eta = \frac{\sigma_{\mathfrak{na}_s}}{\sigma_{\mathfrak{na}}}, \quad \sigma_{\mathfrak{na}_s} \begin{cases} \frac{1}{N_{GB}} \sum_{k=1}^{N} \sigma_{xz}^{+max,k}, & \frac{1}{N_{GB}} \sum_{k=1}^{N} \sigma_{xz}^{-max,k} \\ \frac{1}{N_{GB}} \sum_{k=1}^{N} \sigma_{yz}^{+max,k}, & \frac{1}{N_{GB}} \sum_{k=1}^{N} \sigma_{yz}^{-max,k} \end{cases} . \tag{24}$$

The shear component of the nano and micro scales are $\sigma_{\mathfrak{na}_s}$ and $\sigma_{\mathfrak{m}_s}$, respectively. Assuming that the ratio η keeps constant through the scaling, $\sigma_{\mathfrak{m}_s} = \eta\sigma_{\mathfrak{m}}$,

where $\sigma_{\mathfrak{na}_s}$ is known from the MD model. In Table 7, the average values used to scale the data from the shear tests are presented, showing very similar results for the four cases.

	$\mathcal{D}_{\mathfrak{na}}$	$\sigma_{\mathfrak{na}_s}$	$\mathcal{D}$	$\mathcal{D}_{\mathfrak{m}}$	$\sigma_{\mathfrak{m}_s}$	η
$(xz)^+$	0.0529	3.61	1	100	0.162	0.331
$(xz)^-$	0.0529	3.58	1	100	0.161	0.329
$(yz)^+$	0.0529	3.60	1	100	0.162	0.330
$(yz)^-$	0.0529	3.60	1	100	0.161	0.330

Table 7: Limit scaling values for shear tests, length expressed in (μm) and stress in (GPa).

735 After the scaling process and the evaluation of the area under the scaled shear stress-strain curves, results of the four cases of shear strain energy density are shown in Figs. 16 and 17. The scattered trend of the energy values caused by the variation of the crystalline orientations of the GBs from $\Sigma 3$ to $\Sigma 81$ can be appreciated.

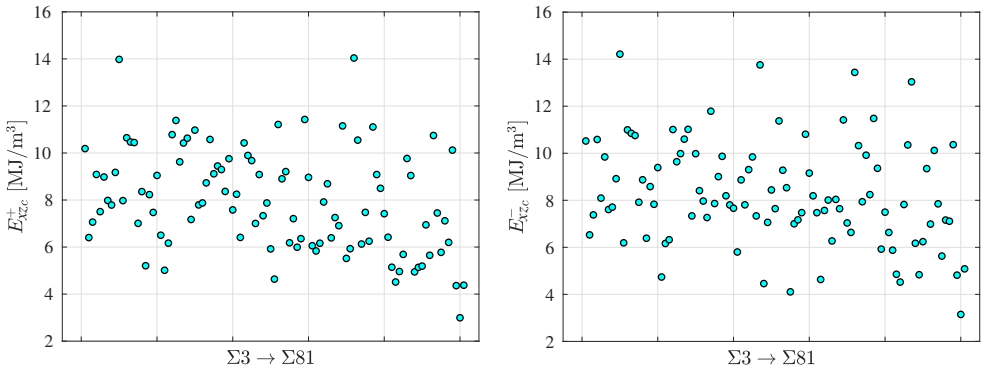

Figure 16: Critical shear energy densities: (a) $E^{+}_{xz_c}$ and (b) $E^{-}_{xz_c}$, both depending on the GB structure.

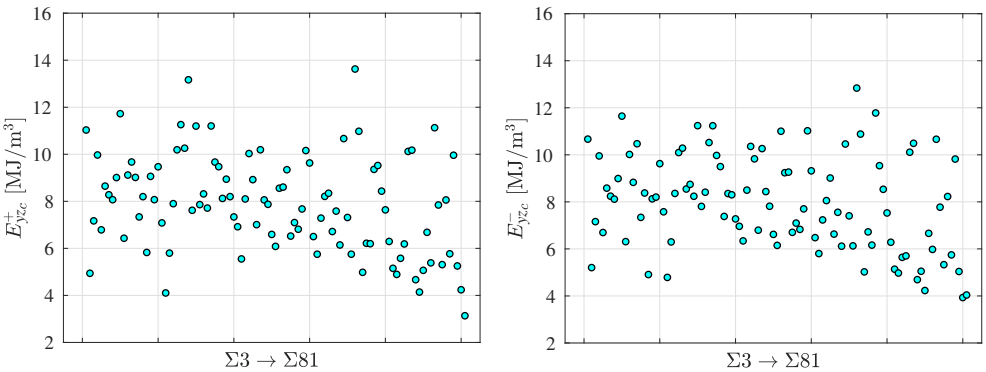

Figure 17: Critical shear energy densities: (a) $E^{+}_{yz_c}$ and (b) $E^{-}_{yz_c}$, both depending on the GB structure.

740 Some differences can be seen between the specific shear modes in both the positive and negative directions of the applied load. The maximum shear critical energy found was $E^{-}_{yz_c} = 14.21\,\mathrm{MJ/m^3}$ and the minimum limit is $E^{+}_{xz_c} = 2.99\,\mathrm{MJ/m^3}$.

Comparing these energies to the cleavage critical energy, an important fact is captured from these results. The defects caused by the transitional lattice in the interfaces reflect a preference to fail under the slip condition in the GB plane.

4.3. Generalized energy failure criterion

The nanoscopic model revealed how the role of the GBs is important for the failure phenomenon, which can affect the overall mechanical behavior of the polycrystalline material. This aspect is relevant for the intergranular modeling, in which several methods can be used to predict failure in different modes. In this first multiscale approach between BEM and MD, the generalized energy failure criterion described by Qu et al. [16] is adapted to a three-dimensional analysis. This criterion is based on the critical energy densities for cleavage and shear modes. The critical energy densities act as threshold properties for each specific GB. This criterion becomes a simple way to evaluate damage at interfaces if the critical energies are previously known from experiments or numerical simulations. As mentioned, the MD modeling used in this work offers a great advantage in the evaluation of all these threshold material properties, including some additional physics aspects.

Based on the classical Rankine criterion, the cleavage failure requires energy to break the atomic bonds forming new crack surfaces and ideally corresponds to the elasticity limit state or the well-defined brittle failure. Otherwise, in the Tresca criterion, shear deformation also needs the energy to activate the plastic regime leading to a ductile failure. Therefore, both Rankine and Tresca criteria might be essentially energy criteria. Hence a simple failure criterion, as shown in Eq. (25), was proposed and validated in [16] in order to predict failure considering

the shear and cleavage mechanisms.

$$\frac{E_s}{E_{sc}} + \frac{E_n}{E_{nc}} = d \quad . \tag{25}$$

In Eq. (25), E_{sc} and E_{nc} represent the previously defined critical energy densities for cleavage and shear conditions. The term d is the damage which lies between 0 and 1. The failure process takes into account both modes on the most critical crystalline plane, that in this case correspond to the GB plane. It can be observed in Fig 14 that the failure processes are not perfectly linear. Owing to the presence of the central crack, while the loading is imposed the material strength is progressively reduced, this is quantified by the dissipative energy density [76]. Furthermore, for some of the GBs used in this work, the plastic regime can appear during the process, making it necessary to evaluate the plastic energy density. Additionally, the quasi-linear behavior from 0 GPa to the σ^{max} corresponds to the elastic energy density. Considering all these regimes, each energy density can be simply represented by the integration under the curves as presented in Fig 14. Hence, the energy densities presented in Figs. 15, 16, and 17 contain the elastic, plastic and dissipative regimes in different proportions according to the GB structure. Applying Eq. (25) for each shear case, the following four failure criteria, Figs. 18 and 19, can be graphically represented.

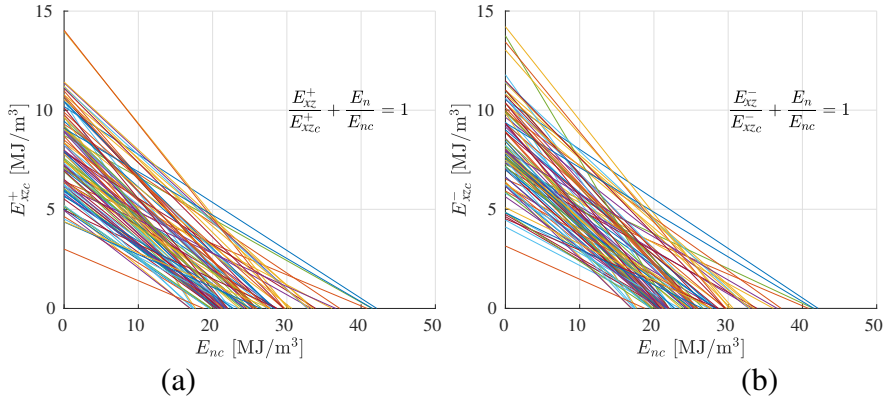

Figure 18: Energy failure diagram: (a) *cleavage-shear* (xz^+) and (b) *cleavage-shear* (xz^-). Each line corresponds to a GB configuration and colors are purely illustrative.

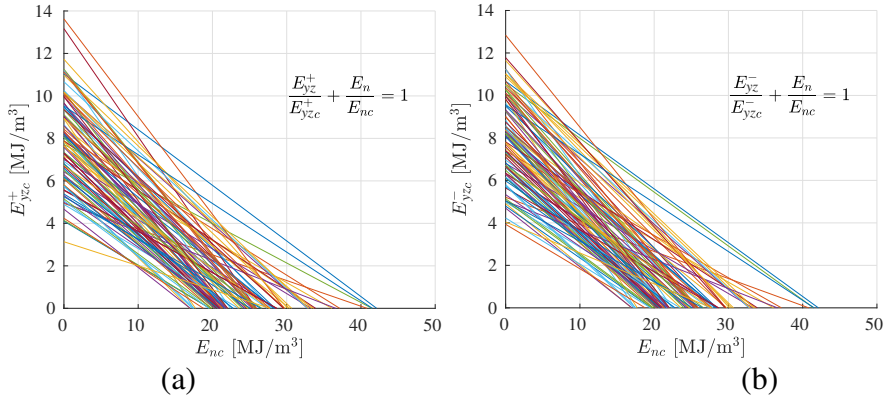

Figure 19: Energy failure diagram: (a) *cleavage-shear* (yz^+) and (b) *cleavage-shear* (yz^-). Each line corresponds to a GB configuration and colors are purely illustrative.

Below each failure line in the energy diagrams, the Fe should always be safe. Notice that, some differences can be perceived between the failure lines of the *xz* or *yz* cases. Qu et al. [16] suggest the definition of the ratio $\varphi = E_{sc}/E_{nc}$ as a parameter that determines the inherent failure mechanism of a material. If $\varphi > 1$, failure is mainly governed by cleavage, indicating that the material is more brittle

than the contrary case $\varphi < 1$, in which the shear failure is predominant and more deformation must be applied to reach the failure condition. The φ limits obtained in this model are presented in Table 8.

Case	φ_{Max}	φ_{Mean}	φ_{Min}
(xz^+)	0.600	0.320	0.156
(xz^-)	0.625	0.334	0.157
(yz^+)	0.554	0.319	0.113
(yz^-)	0.554	0.321	0.127

Table 8: Limits of φ ratio.

According to the previous results, the failure of Fe is dominated by the shear condition. This agrees with some reference values shown in [16], comparing the ratio φ, e.g. for carbon steel (0.55 wt% C) it varies from 0.18 to 0.61. This criterion shows to be useful to predict failure considering both basic mechanisms. It is worth noting that, for GB structures, it is not necessary to find the most critical crystalline plane, since it is implicitly the same GB plane. Furthermore, a detailed extension was considered here to include the two shear directions in a 3D analysis.

4.4. Integranular failure

The final stage of the proposed BEM-MD multiscale approach is illustrated to predict the intergranular failure of polycrystalline Fe at the mesoscale. The damage level is assessed in the interfaces of the polycrystal aggregate by the implementation of the energy failure diagrams at every time and load steps. As mentioned before, this is a continuum model with stochastic crystalline orientations and grain shapes. Hence, infinite possibilities of transition lattice structures

can appear in the grain boundaries. For this reason, it is a difficult task to identify the exact *tilt*, twist or mixed type of misorientation. Then, if a very large sample of atomic GB structures is considered, a more significant failure interval can be obtained, which could be statistically applied along the structure.

Reminding the elastic constants of polycrystalline Fe, $C_{11} = 230\,\text{GPa}$, $C_{12} = 135\,\text{GPa}$ and $C_{44} = 171\,\text{GPa}$ [77] in the reference crystalline orientation. The mesoscale failure is studied on an artificial 80 grains polycrystalline structure, using $163,800$ DOF, Fig. 20. Adequate mesh refinement is required to correctly evaluate the distribution of the stress and strain fields because the energy failure criterion cannot assess the progressive separation process. This structure contains 373 grain boundaries, being necessary to repeat at least 3 times the 101 failure criteria through the material.

According to physical concepts previously exposed to these materials, some parameters must be established for simulations. As mentioned, the mechanical properties were scaled between nano to microscale limits up to $100\,\mu$m. Then, an adequate intermediate size must be defined for the polycrystal specimen. In the dynamic BEM formulation, the time step $\Delta\tau$ is directly related to the incidence of matrices, Eqs. (16), (17) and (18). Hence, both the dimensions and $\Delta\tau$ are fitted simultaneously. After several trials, applying a fully constraint condition at $z = 0$ and a stress-rate of $\dot{\sigma}_{zz}$ at $z = L_z$, the minimum specimen size reached was $L_x = 15\,\mu$m, $L_y = 15\,\mu$m and $L_z = 65\,\mu$m with $\Delta\tau = 5\,$ns. Using these dimensions, and the mesh density of 1.5 [7], an average length of each boundary element was obtained as approximately $1\,\mu$m, as employed in the asymptotic scaling approach, Fig. 20. The large number of elements used in this model numerically benefits the reduction of the time step.

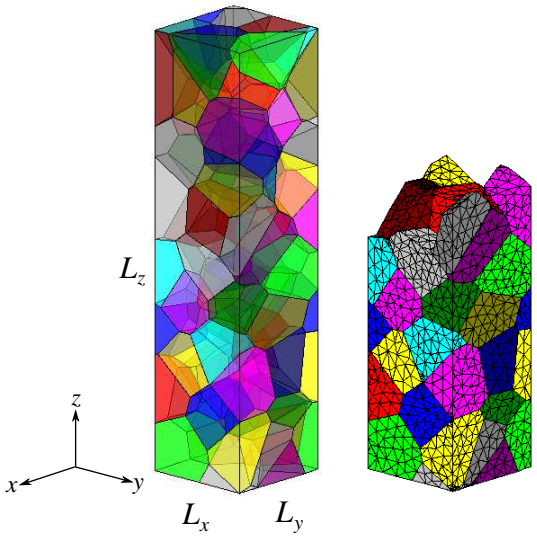

Figure 20: Artificial 80 grains polycrystalline structure, discretized with 18,200 boundary elements.

As previously discussed, other important factors that contribute to the increment of yield strength are the dynamic boundary conditions. In addition, it can be inferred from the specimen size that the average grain-size will be less than $10\,\mu$m. From the literature, very small grain-sized polycrystalline or nanocrystalline materials exhibit strong mechanical properties and elastic regime [78, 79]. This is an advantageous fact because the constitutive model only considers elastic deformation. Although this is not a nanocrystalline model with a yield strength about 5 GPa as simulated by Tong et al. [80], a higher elastic regime interval can be assumed compared to the limit found by Sakui and Sakai [75] for a $10\,\mu$m grain-size Fe. Therefore, in the failure process assessment, the use of small grain sizes can justify the imposition of higher deformation, reducing the possibilities to violate the crystal plasticity phenomenon.

The damage is measured at each interface through the simulation time. The

generalized failure criteria shown in Figs. 18 and 19 is incorporated at the interfaces. Next, at each time step, the energy density is evaluated in each node in the local coordinate system, applying the same $(z-x-z)$ rotation convention that was used for the distribution of the crystalline orientations. Owing to the non-linear deformation gradient caused by the high-stress rate, it is not feasible to compute the energy density as usual for quasi-static models. Therefore, an approximation of the accumulated energy density over time at the kth node is given by

$$E_{ij}^{k}(t_{n+1}) = \sum_{n=1}^{N_c} E_{ij}^{k}(t_n) + E_{ij}^{k} \quad , \tag{26}$$

where N_c is the number of time steps, and $ij = xz, yz, zz$ at the local coordinates of each interface. The E_{ij}^{k} term is the current energy assessed as follows

$$E_{ij}^{k} = \begin{cases} \dfrac{1}{2}\left[\sigma_{ij}^{k}(t_{n+1}) + \sigma_{ij}^{k}(t_n)\right]\left[\varepsilon_{ij}^{k}(t_{n+1}) - \varepsilon_{ij}^{k}(t_n)\right] & \text{if} \quad \begin{cases} \sigma_{ij}^{k}(t_{n+1}) > \sigma_{ij}^{k}(t_n) \\ \varepsilon_{ij}^{k}(t_{n+1}) > \varepsilon_{ij}^{k}(t_n) \end{cases} \\ E_{ij}^{k}(t_n) & \text{if} \quad \text{other case} \end{cases} , \tag{27}$$

being σ_{ij}^{k} and ε_{ij}^{k} the stress and strain nodal values. If the deformation increases through time at the kth node, growth is expected in the stored energy that can be interpreted as damage accumulation when the failure criterion Eq. (25), is applied. For that reason, in order to contemplate the irreversible failure process, if the material point is not deformed at some instant, the stored energy remains constant with its value at the last time step. For illustrative purposes, this simulation procedure can be observed in Fig. 21.

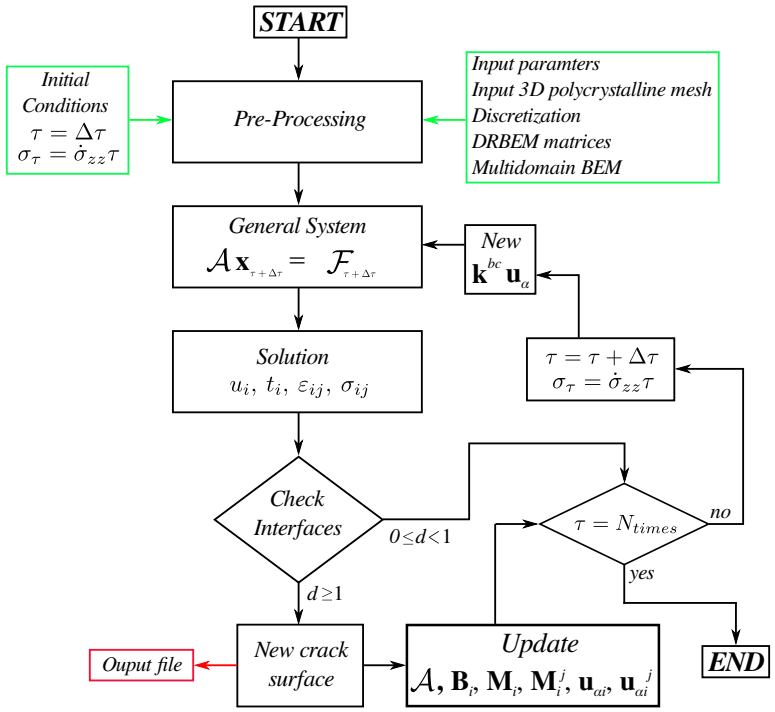

Figure 21: Failure algorithm.

After the first step solution, all the interfaces must be checked node by node if they are under traction load, $\sigma_{zz} > 0$. In case of the compressive load $\sigma_{zz} < 0$, it is assumed that $E_n = 0\,\mathrm{MJ/m^3}$. Then, in that case, the failure is characterized by the slip condition, because of $E_s > 0$. For the shear cases, it is selected the most critical energy between the $x^{\pm}$ and $y^{\pm}$ local axes. When the pair is totally damaged $d = 1$, the general $\mathcal{A}$ matrix and the $\mathcal{F}$ vector are updated. Owing to the dynamic formulation requiring the displacement response of the last three time steps, the new independent nodes will have the same displacement information for the next time step. Therefore, it is also necessary to update the vector $\mathbf{u}_\alpha$. Finally, for the new time and load steps, the vectors of boundary conditions $\mathbf{k}^{bc}$ and $\mathbf{u}_\alpha$ are updated. Next, an intergranular failure simulation is carried out using

the 80 grain polycrystal aggregate shown in Fig. 20. In this case, the stress-rate $\dot{\sigma}_{zz} = 10\,\text{MPa/ns}$ is imposed at $z = L_z$ and again, the base $z = 0$ is fully constrained. In this failure test, owing to the elastic BEM formulation used in this work, a pre-crack was initially created in order to reduce the ductile failure mechanism and plastic regime required to reach the crack onset, which will be mainly governed by brittle failure with less deformation level. All interfaces within a defined volume were disconnected forming a weak zone to induce crack propagation, Fig. 22.

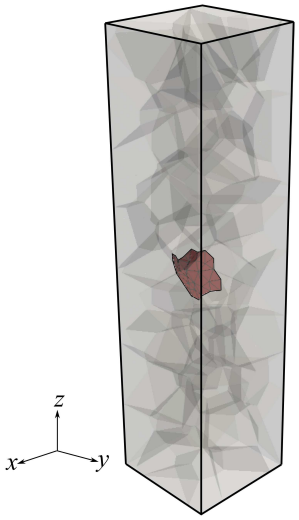

Figure 22: Initial cracked model.

For different instants of time, the damage evolution can be appreciated in Figs. 23 and 24. The complete simulation can be appreciated in the supplementary material item C.

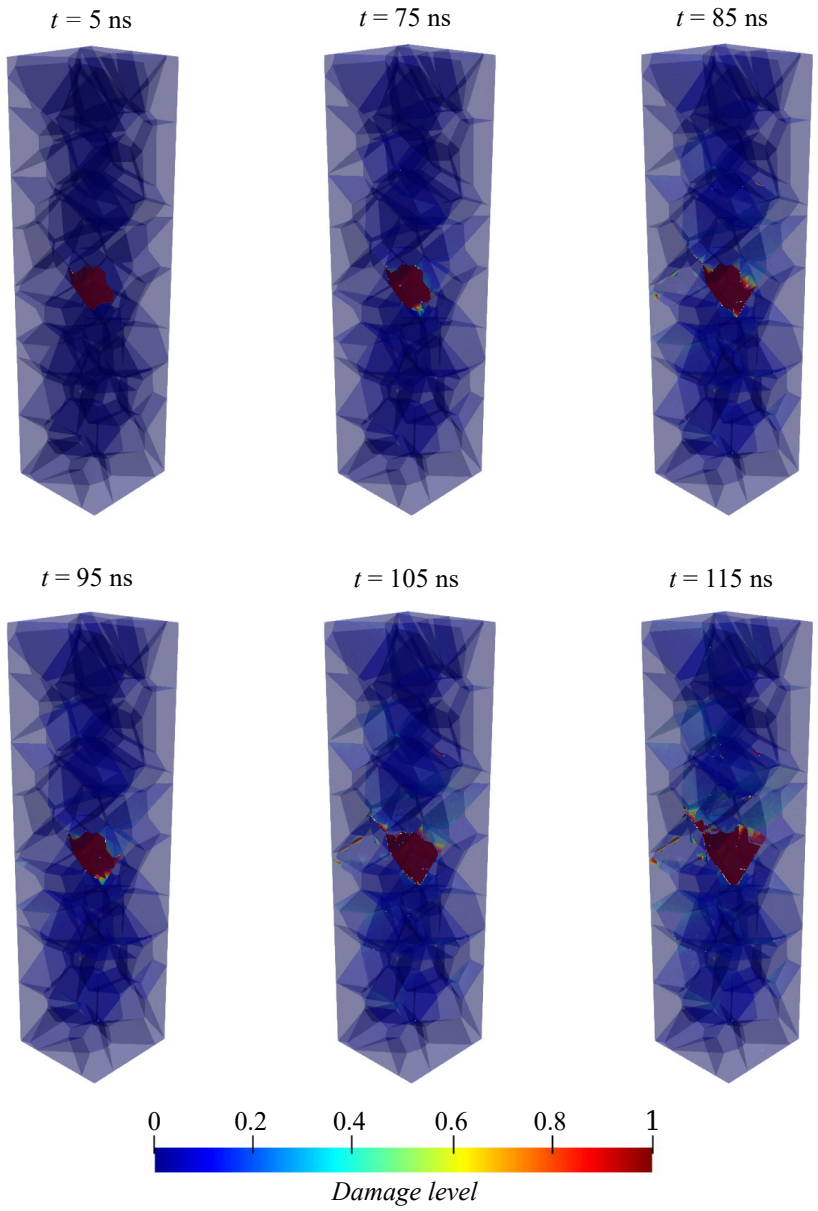

Figure 23: Failure propagation and damage evolution, from 5 ns to 115 ns.

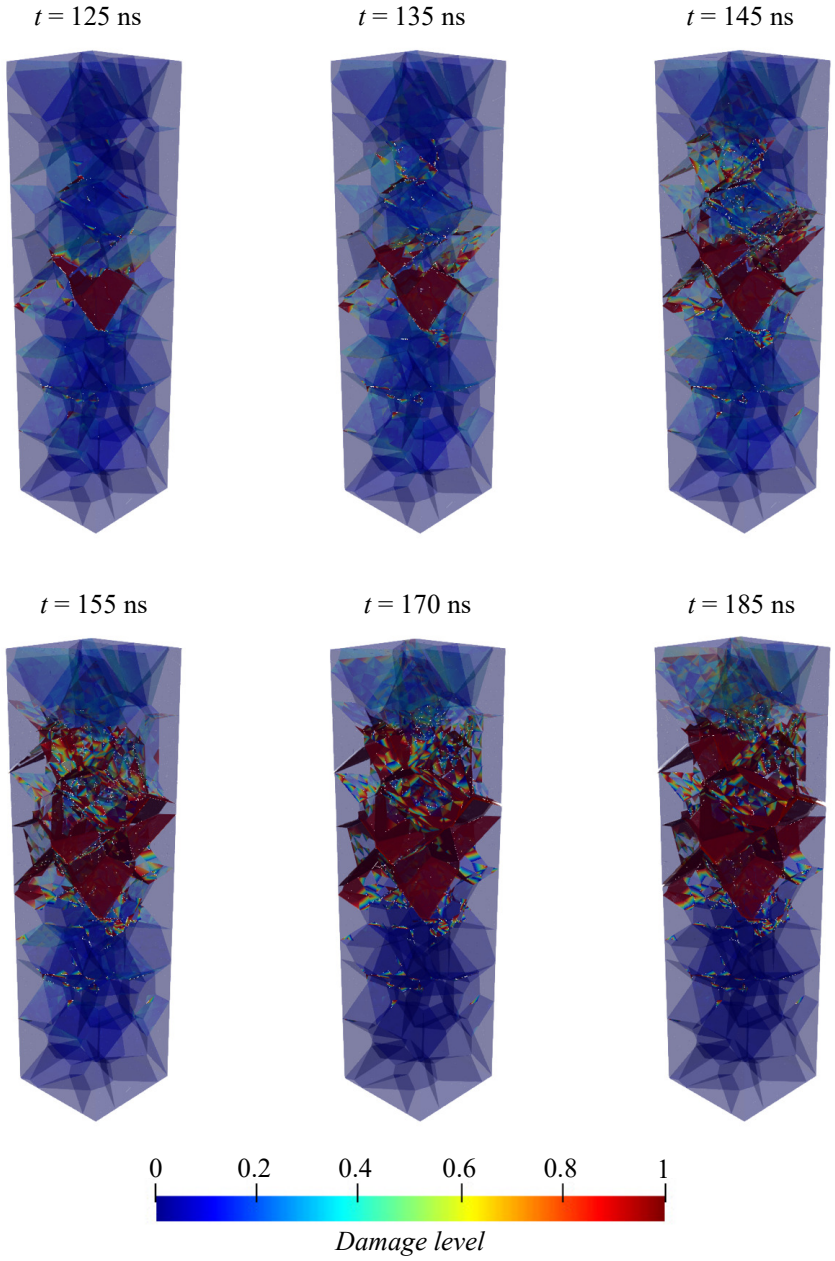

Figure 24: Failure propagation and damage evolution, from 125 ns to 185 ns.

Despite the linear interpolation of the boundary elements used in the present

formulation, the damage variation from 0 to 1 with a color distribution from blue to red is represented for each node. The pre-crack was intentionally located far enough from the boundary, to avoid the influence of the boundary conditions on the failure behavior. The failure initiation at the pre-cracked borders, e.g. at 75 ns can be observed in Fig. 23 . After this time, the failure propagates through the weak zone produced by the initial crack from 75 ns to 105 ns, Fig. 23. The deformation level induces failure in additional interfaces for the higher loads and times from 125 ns onwards, Fig. 24. Furthermore, the failure criterion established that the failure is more likely to occur under shear loading. This fact was reflected in the obtained results, where the propagation path takes place on tilted interfaces. The sudden failure onsets after 60 ns where the homogenized macro-stress is about 600 MPa, Fig. 25(a).

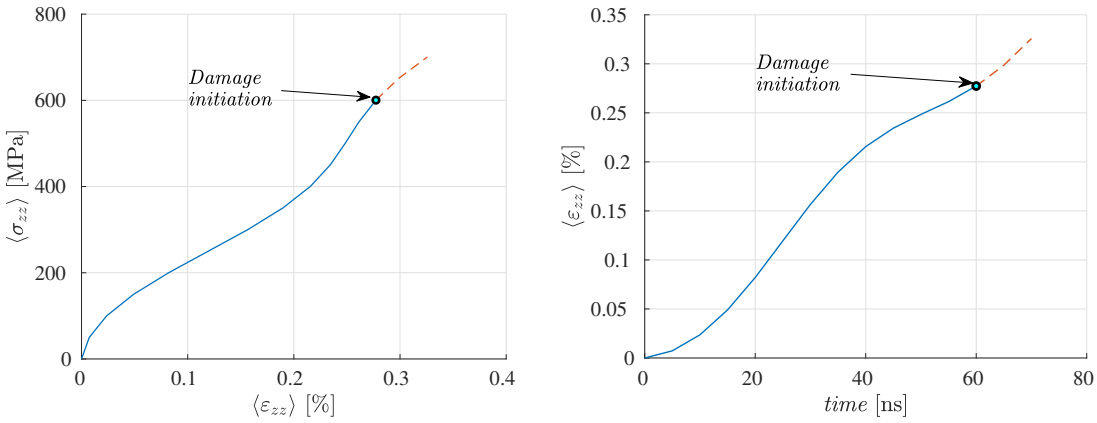

(a) (b)

Figure 25: Macroscopic behavior: (a) constitutive stress-strain relationship and (b) overall deformation as a function of time.

Due to the application of a very high stress-rate, the inertial effects of mass

caused that the elastic regime becomes non-linear. As mentioned, the stress and strain waves progressively propagate through the structure. At the beginning of the time, only a small percentage at the top of the bar is experimenting deformation. If the load is rapidly incremented, the strain wave reflection is not able to comprise the entire specimen length, Fig 25(b). The wave propagation can be easily perceived and the total displacement field is observed as illustrated in Figs. 26 and 27. The complete simulation can be appreciated in the supplementary material item C.

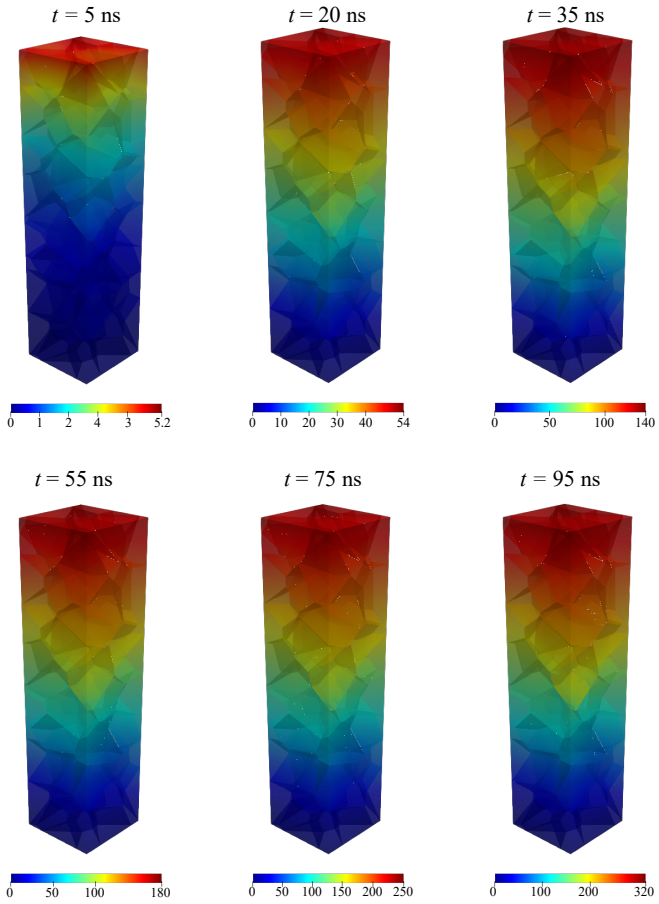

Figure 26: Total displacement from 5 ns to 95 ns, units in (nm).

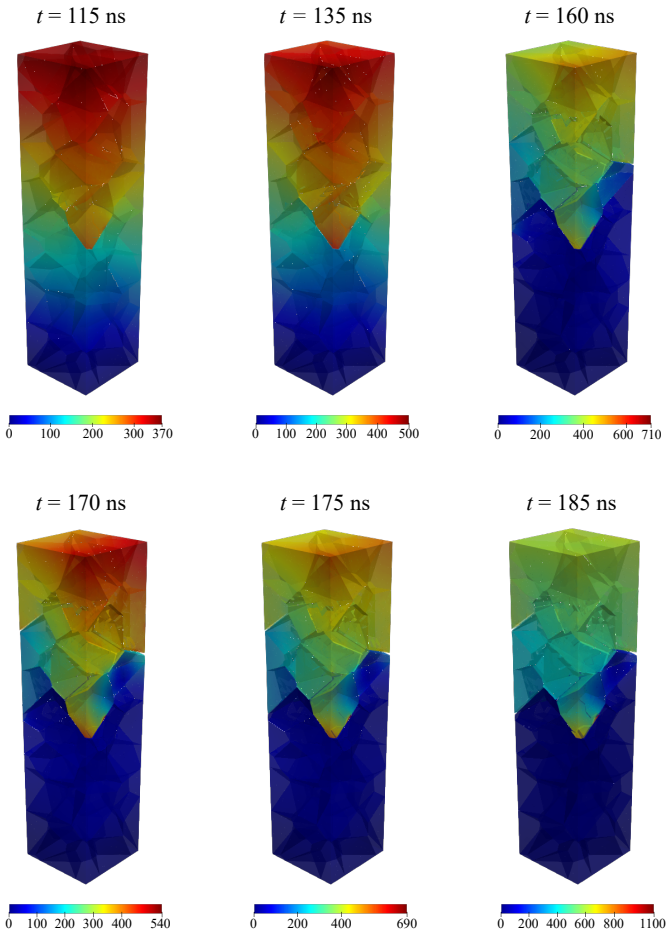

Figure 27: Total displacement from 115 ns to 185 ns, units in (nm).

It is worth noting that before 20 ns, the pre-crack is not suffering significant deformation, as the strain wave has not reached that point in the specimen. After 115 ns, specimen separation is more critical owing to the damage level, and also because the stress-rate is not adaptive as commonly used in cohesive analyses. As shown in Figs. 25(a) and (b), the damage initiates at a deformation of 0.3% and the maximum deformation at 185 ns is 0.85%. This deformation interval is high for considering the elastic regime of metallic materials from a quasi-static

point of view. Despite the lack of other numerical or experimental results for validation, it can be inferred that the imposition of the stress-rate and length size facilitates the increment of the yield strength, as previously explained. Moreover, if a small stress-rate is uniformly imposed, the final deformation at 185 ns will tend to decrease, because of the sudden propagation behavior. In Fig. 28, the failure is shown at the last simulation time of 185 ns.

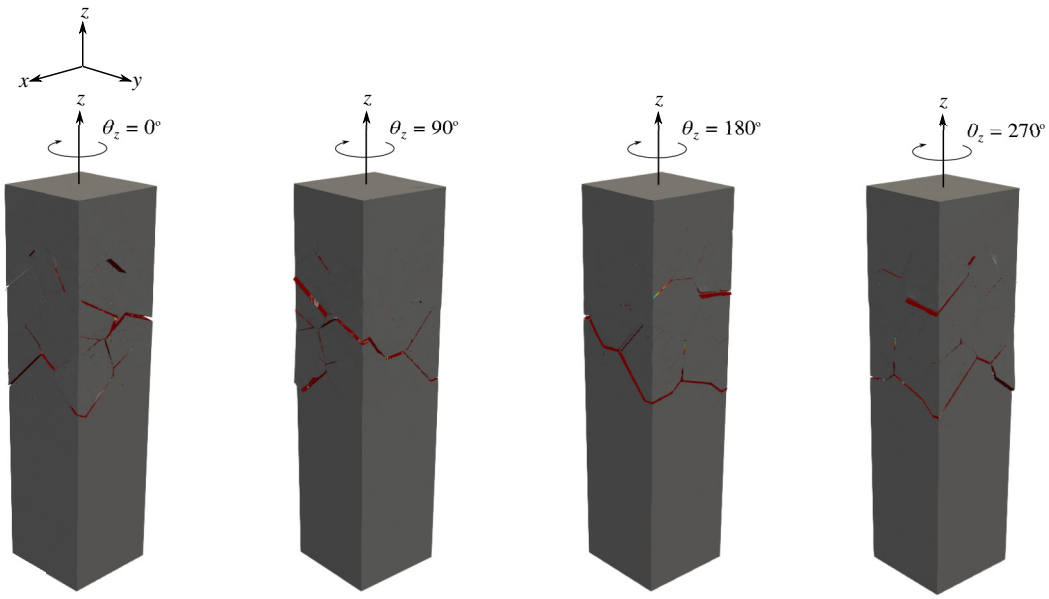

Figure 28: Different views of failure at 185 ns.

In terms of implementation, the coupling of the failure criterion to the mesoscale does not represent any additional computational efforts, because the incidence matrices remain constant along the simulations. Furthermore, the general matrix assembly after each pair separation does not require considerable processing time, even being a serial section of the general BEM algorithm. The solution of the system of equations is carried out using a Multifrontal Massively

Parallel Sparse (MUMPS) [81, 82] direct solver. The code and user's guide are available in http://mumps.enseeiht.fr/. MUMPS implements a direct method based on a multifrontal approach, which performs a Gaussian factorization. This solver is configured for general unsymmetrical real matrices using the out of core option. Additional details of the BEM implementation can be found in [7, 13, 33]. All the parallelized simulation of LAMMPS and BEM presented along this research were run using the *Kahuna Cluster* in the Center for Computational Engineering and Science, see its architecture details in http://cces.unicamp.br/computing-resources/.

5. Conclusions

Intergranular failure at the mesoscale was assessed under dynamic boundary conditions. The failure criterion based on the energy densities was generated considering a sample of 101 GBs using a nanoscale MD model. It evidenced the influence of the crystalline orientation on the critical energy densities for shear and cleavage modes. Moreover, different brittle and ductile failure levels could be analyzed from the GB energy concept, because the GBs with higher energies are directly related to the more ductile nanoscopic specimens. From these results, it was found that the shear slip condition is more critical than cleavage in the GB plane, causing a more rapid failure with less stored energy density. The nanoscale mechanical behavior could not be directly coupled to the microscale model. Then, an asymptotic analysis was employed from models proposed in the literature. It was assumed that all GB results in the nanoscale can compose a heterogeneous random material, constituted as the average of the size length and yield strength of each GB. Therefore, the yield strength was scaled between similar material

structures from nano to microscale. This strategy helped to maintain the scattered character of the GBs to be used in the polycrystal aggregate. The last stage was the incorporation of the complete failure criterion on the mesoscale to finally simulate the intergranular failure. Some basic implementations were required and added to the BEM numerical model. The intergranular failure was predominantly caused by the shear fields at the interfaces. From these results, it can be concluded that the inertia effects caused by the dynamic boundary conditions influence the failure behavior under a non-linear elastic regime.

This multiscale framework offers the possibility to combine the nano- and meso- scales even considering the representative difference in their characteristic lengths. Additional physical phenomena were captured on the continuum mesoscale by the incorporation of the nanoscale modeled using MD. It was demonstrated how the failure processes at interfaces have a relevant influence caused by the resulting lattice structures after two adjacent grains are atomistically collapsed. This fact is considered the enhancement and novelty of this dynamic failure model compared with others in the literature. Therefore, this is a proper approach from a continuum point of view, where the interface failure criteria were generated with the mentioned considerations. For simulating failure in metallic materials from a microscopic standpoint, the proposed model intends harnessing what BEM and MD can provide at each scale. It would be very expensive in terms of computational cost if MD simulations are carried out generating a complete atomic polycrystalline aggregate with a grain size of about $10\,\mu$m. On the other hand, a pure continuum simulation by itself would have a dependency on experimental data for modeling the failure of several metals. Then, the synergy of these methods provides a proper approach for the analysis of polycrystals with large grain size,

even with the level of detail offered by the atomistic modeling.

6. Data availability

The supplementary material required to reproduce these findings are available to download from http://dx.doi.org/10.17632/snm7cx7vvf.1. Instructions for the data acquisition of the meshed polycrystalline structure used in this work are provided. The LAMMPS scripts for the minimization energy and failure tests are described in detail. In order to use these scripts, all the grain boundaries are listed with adequate information to be reproduced using GBstudio. The data for the grain boundary energy and failure criterion are presented in some interactive Matlab® figures. Finally, the simulations of atomistic and mesoscale failure shown in this article are available in the same Mendeley links above.

Acknowledgements

The authors gratefully acknowledge the National Council for Scientific and Technological Development-CNPq (grant numbers: 312493/2013-4, 154283/2014-2), and the Coordination for the Improvement of Higher Education Personnel-CAPES (grant number: 88882.329019/2019-01). Finally, the authors would like to thank the Center for Computational Engineering and Science-CCES at the University of Campinas funded by the São Paulo Research Foundation-FAPESP (Project: 2013/08293-7), for providing access to computational facilities.

This material is based upon work supported by the Air Force Office of Scientific Research-AFOSR under award number FA9550-18-1-0113.

References

[1] C. H. Rycroft, Voro++: A three-dimensional Voronoi cell library in C++, Chaos 19 (2009) 041111–1.

[2] R. Quey, L. Renversade, Optimal polyhedral description of 3D polycrystals: Method and application to statistical and synchrotron X-ray diffraction data, Computer Methods in Applied Mechanics and Engineering 330 (2018) 308–333.

[3] V. Gulizzi, C. H. Rycroft, I. Benedetti, Modelling intergranular and transgranular micro-cracking in polycrystalline materials, Computer Methods in Applied Mechanics and Engineering 329 (2018) 168–194.

[4] F. Fritzen, T. Hlke, E. Schnack, Periodic three-dimensional mesh generation for crystalline aggregates based on Voronoi tessellation, Computational Mechanics 43 (2009) 701–713.

[5] R. Brommesson, M. Ekh, C. Joseph, 3D grain structure modelling of intergranular fracture in forged Haynes 282, Engineering Fracture Mechanics 154 (2016) 57–71.

[6] C. L. Tan, Y. C. Shiah, C. Y. Wang, Boundary element elastic stress analysis of 3D generally anisotropic solids using fundamental solutions based on Fourier series, International Journal of Solids and Structures 50 (2013) 2701–2711.

[7] A. F. Galvis, R. Q. Rodriguez, P. Sollero, Analysis of three-dimensional hexagonal and cubic polycrystals using the boundary element method, Mechanics of Materials 117 (2018) 58–72.

[8] I. Benedetti, M. H. Aliabadi, A three-dimensional grain boundary formulation for microstructural modeling of polycrystalline materials, Computational Materials Science 67 (2013) 249–260.

[9] R. Clough, J. Penzien, Dynamic of Structures, Third Edition, Computers & Structures, Inc, Berkeley, 2003.

[10] M. A. Meyers, Dynamic Behavior of Materials, John Wiley & Sons, Inc, New York, 1994.

[11] D. Gross, T. Seelig, Fracture Mechanics With an Introduction to Micromechanics, Springer-Verlag, Berlin, 2006.

[12] E. L. Albuquerque, P. Sollero, M. H. Aliabadi, Dual boundary element method for anisotropic dynamic fracture mechanics, International Journal for Numerical Methods in Engineering 59 (2004) 1187–1205.

[13] A. F. Galvis, R. Q. Rodriguez, P. Sollero, Dynamic analysis of three-dimensional polycrystalline materials using the boundary element method, Computers & Structures 200 (2018) 11–20.

[14] T. Luther, C. Könke, Coupled cohesive zone representations from 3D quasicontinuum simulation on brittle grain boundaries, International Journal for Multiscale Computational Engineering 9 (4) (2011) 481–501.

[15] B. Ren, S. Li, A three-dimensional atomistic-based process zone model simulation of fragmentation in polycrystalline solids, International Journal for Numerical Methods in Engineering 93 (2013) 989–1014.

[16] R. T. Qu, Z. J. Zhang, P. Zhang, Z. Q. Liu, Z. F. Zhang, Generalized energy failure criterion, Scientific Reports - Nature 6 (2016) 23359–8.

[17] M. F. Horstemeyer, M. I. Baskes, S. J. Plimpton, Length scale and time scale effects on the plastic flow of FCC metals, Acta Materialia 49 (2001) 4363–4374.

[18] M. F. Horstemeyer, M. I. Baskes, Atomistic finite deformation simulations: A discussion on length scale effects in relation to mechanical stresses, Journal of Engineering Materials and Technology 121 (2) (1999) 114–119.

[19] Y. Guo, Z. Zhuang, X. Y. Li, Z. Chen, An investigation of the combined size and rate effects on the mechanical responses of FCC metals, International Journal of Solids and Structures 44 (2007) 1180–1195.

[20] F. Hammami, Y. Kulkarni, Rate dependence of grain boundary sliding via time-scaling atomistic simulations, Journal of Applied Physics 121 (2017) 085303–5.

[21] H. Gao, Y. Huang, W. D. Nix, J. W. Hutchinson, Mechanism-based strain gradient plasticity-I. Theory, Journal of the Mechanics and Physics of Solids 47 (1999) 1239–1263.

[22] Z. P. Bazant, Scaling of dislocation-based strain-gradient plasticity, Journal of the Mechanics and Physics of Solids 50 (2002) 435–448.

[23] Z. Chen, L. Shen, H. E. Fang, Hypersurface for the combined loading rate and specimen size effects on material properties, International Journal for Multiscale Computational Engineering 3 (4) (2005) 451–461.

[24] Z. Chen, Y. Gan, L. M. Shen, Multiscaling in Molecular and Continuum Mechanics: Interaction of Time and Size from Macro to Nano, Springer, 2007, Ch. Combined loading rate and specimen size effects on the material properties, pp. 67–84.

[25] S. Plimpton, Fast parallel algorithms for shortrange molecular dynamics, Journal of Computational Physics 117 (1995) 1–19.

[26] C. H. Rycroft, G. S. Grest, J. W. Landry, M. Z. Bazant, Analysis of granular flow in a pebble-bed nuclear reactor, Physical Review 74 (2006) 021306–16.

[27] C. H. Rycroft, Multiscale modeling in granular flow, Ph.D. thesis, Massachusetts Institute of Technology (2007).

[28] J. R. Shewchuk, Applied Computational Geometry Towards Geometric Engineering, Springer, Philadelphia, 1996, Ch. Triangle: Engineering a 2D Quality Mesh Generator and Delaunay Triangulator, pp. 203–222.

[29] I. M. Daniel, O. Shai, Engineering Mechanics of Composite Materials, Oxford University Press, New York, 2006.

[30] J. L. Synge, The Hypercircle in Mathematical Physics, Cambridge University Press, Cambridge, 1957.

[31] D. M. Barnett, The precise evaluation of derivatives of the anisotropic elastic Green's functions, Physics State Solid 49 (1972) 741–748.

[32] T. C. T. Ting, V. G. Lee, The three-dimensional elastostatic Green's function for general anisotropic linear elastic solids, The Quarterly Journal of Mechanics & Applied Mathematics 50 (1997) 407–426.

[33] A. F. Galvis, Multiscale Modeling of Dynamic Failure in 3D Polycrystalline Materials using BEM and MD, Ph.D. thesis, School of Mechanical Engineering, University of Campinas (2019).

[34] R. Q. Rodríguez, A. F. Galvis, P. Sollero, C. L. Tan, E. L. Albuquerque, Fast BEM multi-domain approach for the elastostatic analysis of short fibre composites, European Journal of Computational Mechanics 26 (5-6) (2017) 525–540.

[35] M. Kögl, L. Gaul, A 3-D boundary element method for dynamic analysis of anisotropic elastic solids, CMES: Computer Modeling in Engineering & Science 1 (4) (2000) 27–43.

[36] R. Rodríguez, A. F. Galvis, P. Sollero, C. L. Tan, E. L. Albuquerque, Transient dynamic analysis of generally anisotropic materials using the boundary element method, Acta Mechanica 229 (2018) 1893–1910.

[37] J. C. Houbolt, A reccurrence matrix solution for the dynamic response of elastic aircraft, Journal of Aeronautical and Science 17 (9) (1950) 540–550.

[38] J. Dominguez, Boundary Elements in Dynamics, Computational Mechanics Publications, Southampton, 1993.

[39] E. L. Albuquerque, P. Sollero, M. H. Aliabadi, The boundary element method applied to time dependent problems in anisotropic materials, International Journal of Solids and Structures 39 (2002) 1405–1422.

[40] J. H. Kane, Boundary Element Analysis In Engineering Continuum Mechanics, Prentice-Hall, New Yersey, 1994.

[41] F. Cabané-Brouty, J. Bernardini, Segregation and diffusion, Journal de Physique Colloques 43 (C6) (1982) 163–176.

[42] P. Ballo, Grain boundary sliding and migration: Effect of temperature and vacancies, Physical Review B 64 (2001) 024104–7.

[43] D. Steele, D. Evans, P. Nolan, D. J. Lloyd, Quantification of grain boundary precipitation and the influence of quench rate in 6XXX aluminum alloys, Materials Characterization 58 (2007) 40–45.

[44] B. Q. Li, A. P. Reynolds, Correlation of grain-boundary precipitates parameters with fracture toughness in an AlCuMgAg alloy subjected to long-term thermal exposure, Journal of Materials Science 33 (1998) 5849–5853.

[45] C. L. Briant, Grain boundary structure, chemistry, and failure, Materials Science and Technology 17 (11) (2001) 1317–1323.

[46] P. Lejcek, Grain Boundary Segregation in Metals, Springer Heidelberg, London, 2010, Ch. Grain Boundaries: Description, Structure and Thermodynamics, pp. 5–24.

[47] J. L. Rouvierea, K. Rousseau, F. Fournel, H. Moriceau, Huge differences between low- and high-angle twist grain boundaries: The case of ultrathin (001) Si films bonded to (001) Si wafers, Applied Physics Letters 77 (8) (2000) 1135–1137.

[48] Y. Gao, Z. Jin, Interaction between lattice dislocations and low-angle grain boundaries in Ni via molecular dynamics simulations, Molecular Simulation 43 (2017) 1172–1178.

[49] A. C. Shi, C. Rottman, Y. He, Calculation of energy of low-angle grain boundaries, Philosophical Magazine A 55 (4) (1989) 499–511.

[50] N. H. Fletcher, Advances in Materials Research, Wiley, New York, 1971, Ch. Crystal interface models a critical survey, pp. 281–314.

[51] H. Ogawa, GBstudio: A Builder software on periodic models of CSL boundaries for molecular simulation, Materials Transactions 47 (11) (2006) 2706–2710.

[52] J. D. Rittner, D. N. Seidman, ⟨110⟩ symmetric tilt grain-boundary structures in fcc metals with low stacking-fault energies, Physical Review B 54 (10) (1996) 6999–7015.

[53] M. D. Sangid, H. Sehitoglua, H. J. Maier, T. Niendorf, Grain boundary characterization and energetics of superalloys, Materials Science and Engineering A 527 (2010) 7115–7125.

[54] D. Wolf, Structure and energy of general grain boundaries in bcc metals, Journal of Applied Physics 69 (1) (1991) 185–196.

[55] T. Watanabe, K. I. Arai, K. Yoshimi, Texture and grain boundary character distribution (GBCD) in rapidly solidified and annealed Fe-6.5mass%Si ribbons, Philosophical Magazine Letters 59 (2) (1989) 47–52.

[56] Z. W. Zhang, W. H. Wang, Y. Zou, I. Baker, D. Cheng, Y. F. Liang, Control of grain boundary character distribution and its effects on the deformation of Fe6.5 wt.% Si, Journal of Alloys and Compounds 639 (2015) 40–44.

[57] Y. Zhang, A. Gokhman, W. Wang, Z. Zhang, Effects of annealing on grain-boundary character distribution and texture evolution in hot-rolled Fe-6.5 wt% Si steel, Journal of Magnetism and Magnetic Materials 451 (2018) 187–192.

[58] M. I. Mendelev, S. Han, D. J. Srolovitz, Development of new interatomic potentials appropriate for crystalline and liquid iron, Philosophical Magazine 83 (35) (2003) 3977–3994.

[59] M. E. Tuckerman, J. Alejandre, R. López-Rendón, A. L. Jochim, G. J. Martyna, A Liouville-operator derived measure-preserving integrator for molecular dynamics simulations in the isothermal-isobaric ensemble, Journal of Physics A: Mathematical and General 39 (2006) 5629–5651.

[60] M. A. Tschopp, D. L. McDowell, Asymmetric tilt grain boundary structure and energy in copper and aluminium, Philosophical Magazine 87 (25) (2007) 3871–3892.

[61] M. A. Tschopp, D. L. McDowell, Structures and energies of $\Sigma 3$ asymmetric tilt grain boundaries in copper and aluminium, Philosophical Magazine 87 (22) (2007) 3147–3173.

[62] M. A. Tschopp, K. N. Solanki, F. Gao, X. Sun, M. A. Khaleel, M. F. Horstemeyer, Probing grain boundary sink strength at the nanoscale: Energetics and length scales of vacancy and interstitial absorption by grain boundaries in α-Fe, Physical Review B 85 (2012) 064108–21.

[63] B. Runnels, I. J. Beyerlein, S. C. M. Ortiz, A relaxation method for the

energy and morphology of grain boundaries and interfaces, Journal of the Mechanics and Physics of Solids 94 (2016) 338–408.

[64] R. Dingreville, D. Aksoy, D. E. Spearot, A primer on selecting grain boundary sets for comparison of interfacial fracture properties in molecular dynamics simulations, Scientific Reports - Nature 7 (2017) 8332–12.

[65] V. Yamakov, E. Saether, E. H. Glaessgen, Molecular modeling of intergranular fracture in aluminum: constitutive relation for interface debonding, Journal of Materials Science 43 (2008) 7488–7494.

[66] W. Barrows, R. Dingreville, D. Spearot, Traction-separation relationships for hydrogen-induced grain boundary embrittlement in nickel via molecular dynamics simulations, Materials Science and Engineering: A 650 (2016) 354–364.

[67] T. Schneider, E. Stoll, Molecular-dynamics study of a three-dimensional one-component model for distortive phase transitions, Physical Review B 17 (3) (1978) 1302–1322.

[68] M. Parrinello, A. Rahman, Polymorphic transitions in single crystals: A new molecular dynamics method, Journal of Applied Physics 52 (12) (1981) 7182–7190.

[69] G. J. Martyna, D. J. Tobias, M. L. Klein, Constant pressure molecular dynamics algorithms, The Journal of Chemical Physics 101 (1) (1994) 4177–4189.

[70] W. Shinoda, M. Shiga, M. Mikami, Rapid estimation of elastic constants by

molecular dynamics simulation under constant stress, Physical Review B 69 (2004) 134103–8.

[71] X. Wu, V. Prakash, Dynamic compressive behavior of ice at cryogenic temperatures, Cold Regions Science and Technology 118 (2015) 1–13.

[72] P. Santos-Flórez, C. J. Ruestes, M. de Koning, Uniaxial-deformation behavior of ice I_h as described by the TIP4P/Ice and mW water models, The Journal of Chemical Physics 149 (2018) 164711–8.

[73] B. Paliwal, M. Cherkaoui, An improved atomistic simulation based mixed-mode cohesive zone law considering non-planar crack growth, International Journal of Solids and Structures 50 (2013) 3346–3360.

[74] Z. P. Bazant, Scaling laws in mechanics of failure, Journal of Engineering Mechanics 119 (9) (1993) 1828–1844.

[75] S. Sakui, T. Sakai, The effect of strain rate, temperature and grain size on the lower yield stress and flow stress of polycrystalline pure iron, J-STAGE 58 (10) (1972) 1438–1455.

[76] Q. M. Li, Strain energy density failure criterion, International Journal of Solids and Structures 38 (2001) 6997–7013.

[77] H. B. Huntington, The Elastic Constants of Crystals, Academic Press Inc, New York, 1958.

[78] D. Jang, M. Atzmon, Grain-size dependence of plastic deformation in nanocrystalline Fe, Journal of Applied Physics 93 (11) (2003) 9282–9286.

[79] K. M. Youssef, R. O. Scattergood, K. L. Murty, J. A. Horton, C. C. Koch, Ultrahigh strength and high ductility of bulk nanocrystalline copper, Applied Physics Letters 87 (2005) 091904–3.

[80] X. Tong, H. Zhang, D. Y. Li, Effect of annealing treatment on mechanical properties of nanocrystalline α-iron: an atomistic study, Nature: Scientific Reports 5 (2015) 8459–7.

[81] P. R. Amestoy, I. S. Duff, J. Koster, J.-Y. L'Excellent, A fully asynchronous multifrontal solver using distributed dynamic scheduling, SIAM Journal on Matrix Analysis and Applications 23 (1) (2001) 15–41.

[82] P. R. Amestoy, A. Guermouche, J.-Y. L'Excellent, S. Pralet, Hybrid scheduling for the parallel solution of linear systems, Parallel Computing 32 (2) (2006) 136–156.